Remote Sensing Applications: Society and Environment 31 (2023) 101004

Contents lists available at ScienceDirect

Remote Sensing Applications: Society and Environment

journal homepage: www.elsevier.com/locate/rsase

Earthquake spatial probability and hazard estimation using various explainable AI (XAI) models at the Arabian peninsula

Ratiranjan Jena [a, *], Abdallah Shanableh [a, b], Rami Al-Ruzouq [a, b], Biswajeet Pradhan [c, d], Mohamed Barakat A. Gibril [a, b], Mohamad Ali Khalil [a], Omid Ghorbanzadeh [e, f, **], Pedram Ghamisi [e, g]

[a] GIS & Remote Sensing Center, Research Institute of Sciences and Engineering, University of Sharjah, Sharjah, 27272, United Arab Emirates
[b] Civil and Environmental Engineering Department, University of Sharjah, Sharjah, 27272, United Arab Emirates
[c] Centre for Advanced Modelling and Geospatial Information Systems (CAMGIS), School of Civil and Environmental Engineering, Faculty of Engineering and Information Technology, University of Technology Sydney, Australia
[d] Earth Observation Centre, Institute of Climate Change, Universiti Kebangsaan Malaysia, 43600, UKM, Bangi, Selangor, Malaysia
[e] Institute of Advanced Research in Artificial Intelligence (IARAI), Landstraßer Hauptstraße 5, 1030, Vienna, Austria
[f] Institute of Geomatics, University of Natural Resources and Life Sciences, Vienna, Peter-Jordan Strasse 82, 1190, Vienna, Austria
[g] Helmholtz-Zentrum Dresden-Rossendorf, Helmholtz Institute Freiberg for Resource Technology, Machine Learning Group, Chemnitzer Str. 40, 09599, Freiberg, Germany

ARTICLE INFO

Keywords:
Smart explainer
Smart predictor
Local interpretable model-agnostic explanation
Deep learning
Earthquake spatial probability
Hazard

ABSTRACT

Earthquakes are the most destructive natural hazards because of their adversely severe impacts on urban areas. Earthquakes affect people's lives and properties, thus captivating the extensive attention of seismologists. Carrying out probability and hazard assessment for the prevention, and reduction of mega-events and recovery will be of great significance in affected areas. Given that limited studies have attempted to estimate earthquake Spatial Probability Assessment (SPA) in the Arabian Peninsula, this study aims to evaluate the SPA and Earthquake Hazard Assessment (EHA). This study implements and evaluates various machine learning and explainable-AI (XAI) techniques for the estimation of SPA and EHA in the Arabian Peninsula, explores the contribution and highlights the importance of different factors in the development of AI-based models. A total of twelve factors ranging from seismological to geophysical factors were evaluated. Two machine learning models namely Light Gradient Boosting Machine (LightGBM) and deep Recurrent Neural Networks (RNN) along with three XAI approaches (i.e, Smart predictor, Smart Explainer and Local Interpretable Model-Agnostic Explanation (LIME) model) were investigated. Results of the comparative earthquake SPA estimation demonstrated that the accuracy of 89% and 87% were achieved by LightGBM and RNN models. Moreover, the results of the XAI models show that the Smart Predictor provides better spatial outputs than the other evaluated XAI models. The stable factors identified by Smart Predictor were magnitude variation and earthquake frequency whereas the important factors were magnitude variation, earthquake frequency, depth variation, and seismic gap. Collectively, results of SPA show that, the Gulf of Aden, Red Sea, Iran, and Turkey are falling under a very-high SPA index (0.991–1). Correspondingly, Gulf areas, coastal areas of Saudi Arabia, and areas in the Zagros fault and Anatolian fault zone fall under a very-

* Corresponding author.
** Corresponding author. Institute of Advanced Research in Artificial Intelligence (IARAI), Landstraßer Hauptstraße 5, 1030, Vienna, Austria.
E-mail addresses: rjena@sharjah.ac.ae (R. Jena), shanableh@sharjah.ac.ae (A. Shanableh), ralruzouq@sharjah.ac.ae (R. Al-Ruzouq), Biswajeet.Pradhan@uts.edu.au (B. Pradhan), mbgibril@sharjah.ac.ae (M.B.A. Gibril), mkhalil@sharjah.ac.ae (M.A. Khalil), omid.ghorbanzadeh@iarai.ac.at (O. Ghorbanzadeh), pedram.ghamisi@iarai.ac.at (P. Ghamisi).

https://doi.org/10.1016/j.rsase.2023.101004
Received 11 April 2023; Received in revised form 17 May 2023; Accepted 30 May 2023
Available online 1 June 2023

high hazard zone. This research could support planners, and decision-makers for emergency planning, infrastructure development, and reconstruction projects.

1. Introduction

Arabian Peninsula and adjacent regions experienced approximately 3540 earthquakes from 112 to 1998 A.D. ranging in magnitudes (3.5 < mb < 7.0) excludes swarm activities during 1993 and 1995 (Al-Amri, 1998). Historically, the most destructive earthquakes in the Gulf of Aqabah occurred in 1759, 1822, 1837, and 1068 causing 30,000 deaths due to tsunami and building damage. In the dead sea region about 26 major earthquakes (6.1 < ML < 7.3) occurred between 2100 B.C. and 1900 A.D. Almost 68 earthquakes were reported in the northern Red Sea (3.8 < mb < 6.0) from 1964 to 1993 (Al-Amri 1995). The Southern Red Sea reported a total of 170 earthquakes (3.0 < mb < 6.6) for the period 1965–1994. The Zagros-Bitlis fault zone is responsible for numerous earthquakes above 7 + magnitude in the last few decades. Earthquake Spatial probability is defined as the possibility of a spatial distribution of future earthquakes of a certain magnitude in an area. Seismic hazard is defined as the minacious potential of ground shaking, liquefaction, or fault rupture (Reiter 1990). Very few AI-based spatial probability assessments can be seen in the literature (Pourghasemi et al., 2019; Jena et al., 2023; Jena et al., 2020b; Alarifi et al., 2012; Al-Dogom et al., 2021). In recent studies, Probabilistic Seismic Hazard Assessment (PSHA) has been regarded as one of the widely used techniques for earthquake hazard assessments (EHA) (Sulstarova et al., 1980; Grünthal and Leydecker, 1993; Wang 2008). Several EHAs were conducted in Europe through Deterministic Seismic Hazard Assessment (DSHA) and PSHA using seismic activity, geological information, and administrative boundaries.

Pourghasemi et al. (2019) conducted a study on earthquake probability assessment in Iran using an ensemble model and estimated the earthquake spatial probability. Asim et al. (2017) implemented machine learning (ML) techniques with accuracy such as random forest (62%), linear programming booster (65%), pattern recognition neural network (58%), and recurrent neural network (64%) to predict the earthquake magnitude (M ≥ 5.5). Adeli and Panakkat (2009) developed a probabilistic neural network and predicted earthquake magnitudes between 4.6 and 6.0 M*w* with an accuracy of 88%. Schäfer and Wenzel (2019) assessed the potential magnitude and return periods globally using multivariate Ml techniques. Their study showed that major subduction zones have the potential to generate $M_w \geq 8.5$. In recent work, Jena et al. (2020b) conducted an earthquake SPA and EHA study

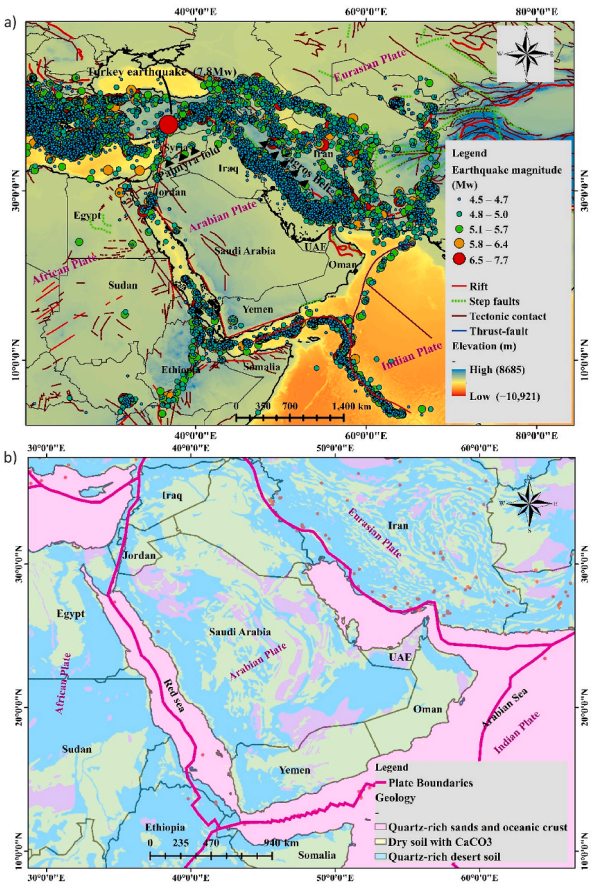

Fig. 1. Study area location of Arabian Peninsula: a) geology of Arabian Peninsula, and b) Tectonic environments and faults.

Table 1
Earthquake catalog and importance of thematic factors for earthquake spatial probability and hazard assessment.

Factors	Thematic layers	Data source	Models	Importance	References
Earthquake catalog	Magnitudes >5 Mw			• Experienced earthquakes used for model training.	USGS
seismological	Slope Elevation Curvature Magnitude variation Depth variation Epicenter density Seismic gap Earthquake frequency	ASTER DEM Earthquake catalog	Machine learning (LightGBM) Smart Predictor, Smart Explainer, and LIME explainable AI Deep learning (RNN)	• Slope, elevation, and curvature controls the crustal faults and landscape processes. • Complicated seismo-tectonics environment could be observed in low and high elevation. • Spatial probability of a certain magnitude could be reflected. • The depth of the source information of events can provide knowledge on a fault zone. • Epicenter density shows the event clusters indicating probability. • Stress accommodation is the reason behind future mega events. • More the earthquake frequency, less the magnitude of event.	Xu and Niu (2018) Alizadeh et al. (2018) Lenhardt (1995) Stoyanov (1993)
Geology	Geology	Landsat 8		• Loose soils cause the seismic amplification.	
Faults	Proximity to thrust faults Proximity to step faults Tectonic contacts density	Landsat ETM+		• Active thrust faults generate high and step faults generate medium magnitude events. • Very high magnitude events often found in the tectonic contacts.	Alizadeh et al. (2018)
Ground motion information	PGA		Probabilistic seismic hazard assessment based various attenuation model.	• Ground motion information used for hazard assessment.	Al-shijbi et al., 2019

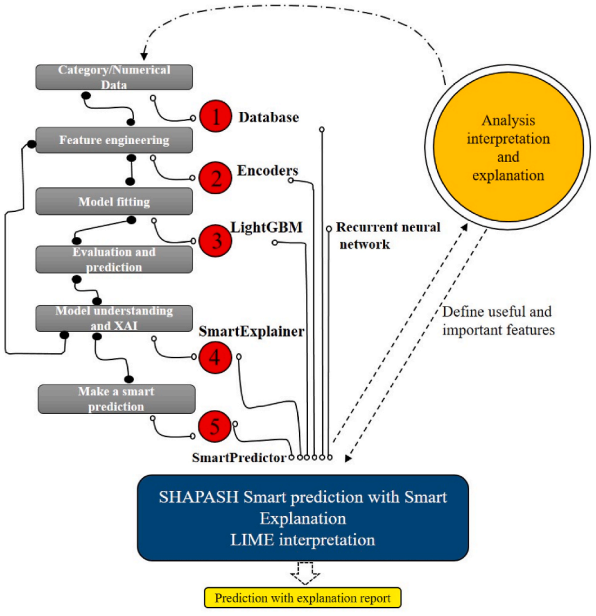

Fig. 2. Methodological flowchart for the earthquake hazard assessment and implementation of Smart Predictor, Smart Explainer, LIME, LightGBM and RNN model.

using clustering and deep learning technique at Palu in Indonesia. Finally, the above study generated risk for land use planning and hazard mitigation purposes at Palu. Beroza et al. (2021) conducted improved earthquake forecasting using ML, which developed a new generation catalog. For EHA, ML, and deep learning models perform excellent prediction and classification (Pourghasemi et al., 2019; Jena et al., 2020b). Alarifi et al. (2012) conducted a successful study on magnitude prediction in the northern Red Sea using an artificial neural network (ANN) that is at least 32% better than other methods. Allahvirdiasl et al. (2022) evaluated the earthquake-induced geo-hazard in Zarand, Central Iran by applying thermal remote sensing techniques. They analyzed an abnormal rise in land surface temperature (LST) due to the earthquake occurrence. Liu et al. (2021) adopted three models namely, support vector machine (SVM), logistic regression (LR), and random forest (RF) to study the quality performance of models for earthquake-induced landslides. Their result demonstrates that RF is a more reliable model because of its ex-

Table 2
Active faults in the Arabian Peninsula with seismic parameters.

Zones	b-value	Magnitude type	Observed magnitude M_{max}^{obs}	Maximum magnitude (M_{max})	σM_{max}	Tectonic environment
Makran subduction zone	0.73	M_w	8.1	8.4	0.27	Subduction zone
Zagros fold belt	0.8	M_w	7.4	7.5	0.12	Fold belt
Dead Sea	1.04	M_w	7.5	7.8	0.45	Subduction and transform fault
Arabian Shield	0.78	M_w	5.7	6.5	0.41	Stable regions
Red Sea	0.62	M_w	7.8	7.9	0.31	Divergent boundary
Gulf of Aden	0.6	M_w	6.6	6.7	0.12	Spreading center
Owen fracture zone	0.56	M_w	7.1	7.2	0.12	Strike slip fault

Table 3
Fault characteristics and ground motion prediction equation (GMPEs) (Adopted from Al-shijbi et al., 2019).

Attenuation models	Mmax	Dist. metric	Dmax	Horizontal component	Faulting mechanism	Tectonic environment
Youngs et al. (1997)	8.2	Rrup	500	Geometric mean	in-slab	Subduction
Atkinson and Boore (2003)	8.3	Rrup	550	Random horizontal	in-slab	Subduction
Atkinson and Boore (2006)	8	Rrup	1000	Unspecified	Unspecified	Stable regions
Zhao et al. (2006)	8.4	Rrup	300	Geometric mean	strike slip fault	Subduction and Shallow active crust
Chiou and Youngs (2008)	8.5	Rrup	200	Average horizontal component	Strike slip fault (reverse and normal)	Shallow active crust
Akkar and Bommer (2010)	7.6	R_{JB}	100	Geometric mean	Strike slip fault (reverse and normal)	Shallow active crust
Campbell (2003)	8.2	Rrup	1000	Geometric mean	Unspecified	Stable regions

cellent performance. Al-Dogom et al. (2021) developed an integrated analytical hierarchical process and ML model for risk mapping followed by earthquake spatial probability and hazard assessment in the United Arab Emirates. In the above studies, it was revealed that the deep learning model outperforms large data sizes when it comes to complex problems than traditional techniques.

Jena et al. (2023) applied an XAI model namely Shapley additive Explanations (SHAP) for earthquake SPA in Arabian Peninsula using a hybrid XGBoost-inception v3 model with an accuracy of 90% and the predictions were explained. Abdollahi and Pradhan (2023) implemented a SHAP model for interpreting the factors of the wildfire susceptibility assessment model. They identified the contributing parameters that impact the prediction model, the reasoning behind the obtained importance, and the output. In another work, Abdollahi and Pradhan (2021) explained how a SHAP model can be utilized to interpret the DNN model implemented for vegetation classification. The model achieved an accuracy of 94.44% by concluding the capability of XAI. These studies provide a more detailed view of the results and their explanations than black box ML models.

The Global Seismic Hazard Assessment Program (GSHAP) is a project which was globally recognized to estimate the peak ground acceleration (PGA) that estimates the maximum intensities in (50yrs, 100yrs, 475yrs, 1000yrs and 2500 years) with the probability of exceedance (Schenk et al., 2000; Sulstarova et al., 1980; Lenhardt 1995; Stoyanov 1993; Grünthal and Leydecker, 1993). Since the 1990s, several PSHA studies were conducted in the Arabian Gulf region (Al-Haddad et al., 1994; Grünthal and Leydecker, 1993; Abdalla and Al-Homoud 2004; Sigbjornsson and Elnashai 2006; Peiris et al., 2006; Malkawi et al., 2007; Aldama-Bustos et al., 2009; Shama 2011; El-Hussain et al., 2012; Khan et al., 2013; Ambraseys et al., 1996; Oliveira et al., 2000; Al-Shijbi et al., 2019). However, limited efforts have been exerted to estimate SPA and EHA on the entire Arabian Peninsula. The two early studies were conducted by Al-Haddad et al. (1992, 1994) to evaluate seismic design criteria for Saudi Arabia and later extended to the entire Arabian Peninsula. The studies implemented a single ground-motion prediction equation (GMPE) and mapped peak ground accelerations (PGA) values for 475 and 2475 years return period; however, a high hazard was observed in the southwestern region of Iran. Pascucci et al. (2008) estimated hazard values for various cities including Dubai, Abu Dhabi, Kuwait, Bahrain, Doha, Jeddah, and Muscat. However, their study did not provide hazard maps for the entire Arabian Peninsula nor consider the active faults of Iran in their seismic source model.

The Arabian Peninsula is growing with population, rapid urbanization, and economic growth in the current period. The Peninsula has attracted many megaprojects (Expo, 2020 in Dubai, Multinational NEUM in Saudi Arabia, Egypt, and Jordan and the World Cup, 2022 in Qatar) (Al-Shijbi et al., 2019). The Lloyd's City Risk Index (2015) demonstrates that approximately US $85 billion of economic output could be at risk because of future earthquakes during the upcoming decade. The AI based models for SPA and EHA are good to mitigate earthquake risk through the enhancement of designs and construction of structures. However, these models are unable to explain the rationale behind a precise prediction. Explainable AI (XAI) is programmed to interpret and explain the model accuracy, fairness, transparency, and outcomes of the prediction models. XAI is mostly discussed with deep learning, and it plays a key role in fairness, accountability and transparency in ML which is beneficial for SPA. Hence, the LIME (Ribeiro et al. 2016) is a local interpretable model agnostic explanation technique used to explain individual predictions. On the same pitch, the Smart Predictor is used to predict the targets at their best to overcome the accuracy based on simple ML models. Hence, end users might not trust the prediction results. Therefore, Smart Explainer was initiated to explain the logic behind certain predictions. Smart Explainer can be ap-

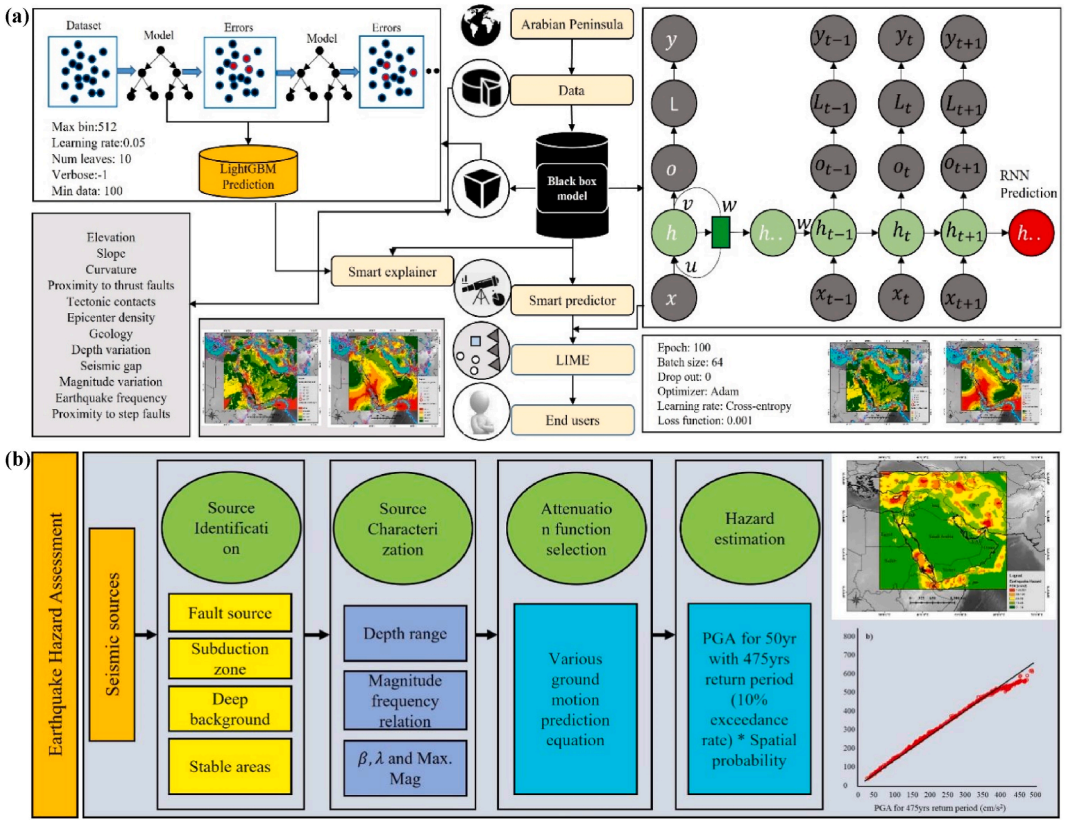

Fig. 3. Model architectures and data flow for hazard assessment.

plied to only ML models, whereas LIME can be implemented in any machine/deep learning model. The basic principle of both is to localize the problem and explain it. A critical literature review suggests that globally, no comprehensive SPA has been conducted using Smart Predictor, Smart Explainer, LIME, and RNN models. There is no description and analysis of the importance of factors being used based on Smart Predictor reports and LIME for SPA. Therefore, the novelty deals with the first-ever study that implemented Smart Predictor and Smart Explainer to estimate earthquake SPA based on the newly developed Shapash python library (Amin et al., 2022; Macedo et al., 2022). This study also implemented an RNN model along with LIME explanation to conduct a comparative assessment with LightGBM-based Smart explainer. The objectives of this study are to (1) apply both machine and deep learning models to produce, update and compare earthquake spatial probability and hazard maps of the Arabian Peninsula; (2) explain and analyze the output of the developed models using XAI technique. A deep Recurrent Neural Network (RNN) model along with LIME explanation were first implemented to conduct a comparative assessment. Moreover, the Smart Explainer and Smart Predictor were also implemented to estimate the importance, interaction, stability, local contribution, capacity, the distance between explanations, and local explanation comparison and predict smartly regarding the information of every factor on a prediction, respectively.

2. Study area

The Arabian Plate formed 25–30 million years ago, leading to the opening of the Red Sea and the Gulf of Aden (Al-Shijbi et al., 2019; Johnson 1998). The earthquakes in Arabian Plate are mostly concentrated along the convergent and divergent boundaries. Three major (the Indian plate, Eurasian plate, and African plate) and two minor plates such as (The Anatolian plate, and the Somalian plate) surround the Arabian plate. The Makran subduction zone developed when the Oman Sea was subducted beneath the Eurasian Plate in Iran and Pakistan (Johnson 1998). The study area location with tectonic characteristics and geology are presented in Fig. 1. The importance of the study area is related to four major issues (active tectonic area, high urbanization rate, economic loss, and a limited number of studies). The selected area is centroid by Arabian Peninsula and adjacent regions, which is unexplored/partially explored that consider the detailed tectonic environment. Limited studies have attempted for a comprehensive SPA in the Gulf of Aden, the Red Sea, which makes this study unique in terms of modern techniques.

The majority of earthquakes in the Arabian Peninsula are concentrated along three major belts namely the Zagros fold belt, the Red Sea and the Gulf of Aqaba. These belts have experienced destructive earthquakes causing huge deaths, landslides, tsunamis, and building damage for a magnitude range of 6–7.5. Comparatively, fewer events were observed in the Makran subduction zone than in any other Benioff zones worldwide, however Makran zone has the potential of ($M_w > 8.0$) that cannot be disregarded (Al-Shijbi et al., 2019). The Zagros–Bitlis Belt length is approximately 1500 km and produces fairly high seismicity. This zone is wide about

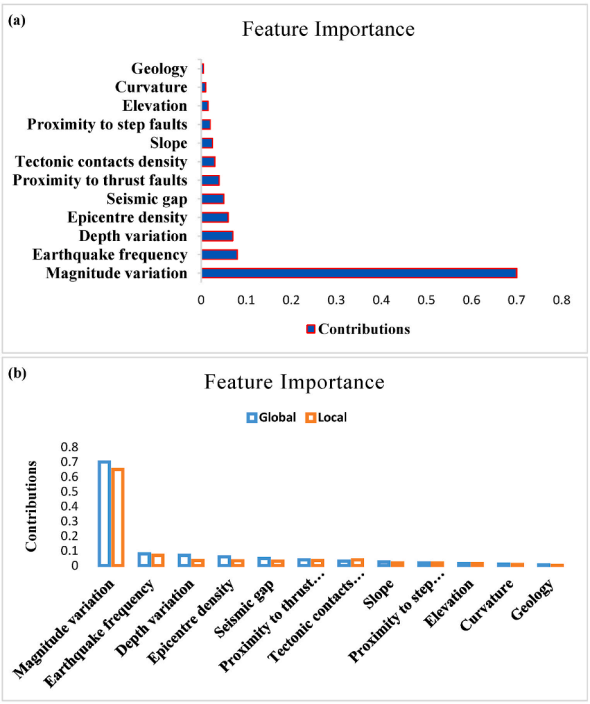

Fig. 4. a) Importance of factors for EHA, b) Comparison of global and local importance of factors for SPA.

200–300 km, accounting for surrounding countries. East Anatolian Fault separates the Anatolian Plate from the Arabian Plate. The length of the East Anatolian Fault is about 600 km. The Gulf of Aqaba–Dead Sea Fault runs about 1100 km, touching the Red Sea and the East Anatolian Fault in the south and north. It is a sinistral plate boundary, portrays the relative movement between the African and Arabian Plates. The inventory earthquakes catalogue shows that events above M_w7.0 have occurred along the entire fault (Deif et al., 2017). The earthquakes in the Red Sea are due to the movement among the African Plate, Gulf of Aden, and Arabian Plate. The damaged earthquakes experienced in Yemen and Saudi Arabia are because of the Red Sea. Geophysical studies in the Gulf of Aden proved the presence of oceanic crust (Coleman 1993). A long 1100-km right lateral fault was formed by the Owen Fracture Zone and the Murray Ridge detaching the Arabian plate from the Indian Plate. The largest earthquake recorded at the Owen Fracture Zone reached to M_w6.6.

3. Geo-potential data acquisition and analysis

3.1. Earthquake catalog and remote sensing images

Various public organizations such as the United States Geological Survey (USGS), the National Earthquake Information Center (NEIC), International Seismological Centre (ISC) and local data from Dubai Seismic Network (DSN) provide open access data for research purposes, with important specifications of magnitudes, depth, and location based on the WGS 84 geodetic coordinates reference system. The earthquake catalog was mainly collected from the USGS portal (earthquake.usgs.gov). A comprehensive catalog that contains data acquired from single and multi-sources were used in the current SPA and EHA assessment. This distributed catalog and digital elevation model (ASTER DEM), geology (Landsat 8), step and thrust faults, and tectonic contacts (Landsat ETM +) were collected from various sources including USGS earth explorer and DIVA-GIS were used to train the model, predict the spatial probability, and generate the hazard map in the present study. The USGS published the seismotectonic atlas (https://pubs.er.usgs.gov/publication/ofr7157), which is an important and authentic referral for seismic source identification. Table 1 below shows the details of data, factors, and their importance for SPA and EHA. In summary, thematic layers were derived from seismological and geotechnical data using GIS based on their importance to generate the spatial probability and hazard maps using AI models.

3.2. Tectonic environments

Local earthquake sources refer to the tectonic environment in the Arabian Peninsula. Earthquake magnitudes are considered in moment magnitude (M_w) in this study. Al-Haddad et al. (1994) conducted a study that documented detailed faults, tectonic contacts, and rift valleys in the Peninsula. Their study shows a geo-structural map representing faults, thrusts, and earthquakes stronger than 4 M_w. The Arabian peninsula's largest tectonic environment is characterized by a subduction zone. The highest b-value can be found in the Dead Sea, while lowest can be observed in the Gulf of Aden. The high magnitude events can be found in tectonic boundaries, whereas the Arabian shield experienced a highest of 5.7 M_w. The maximum magnitude can be experienced in the Makran subduction

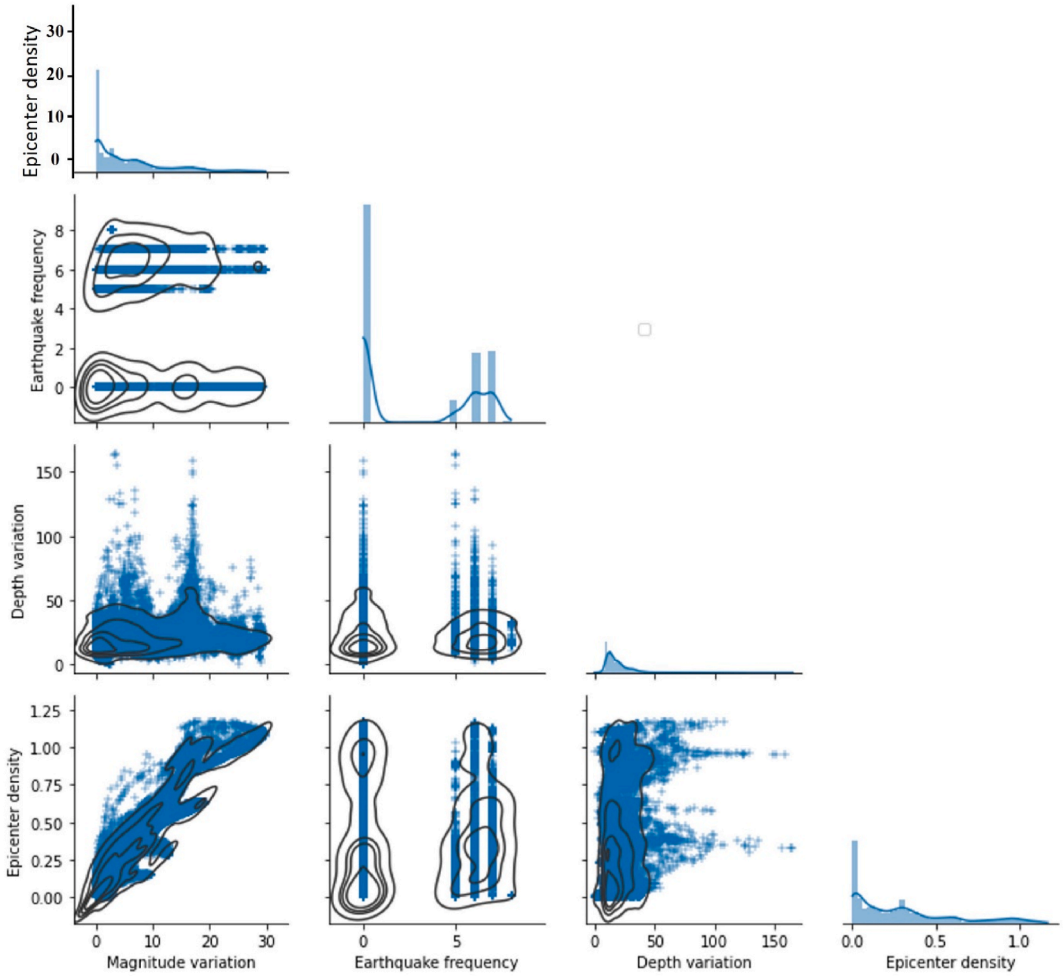

Fig. 5. Correlation among top four factors for spatial probability mapping.

zone is 8.4 M_w. The final hazard map was produced that superimposed all the information through thematic layers. Table 1 summarizes the tectonic environment parameters and their sources.

4. Methodology

Firstly, the study developed the database and derived the thematic layers as the conditioning factors for probability assessment. Numerical data types were produced using GIS. Then, the study implemented encoders as feature engineering, and lightGBM as the prediction models to estimate the earthquake spatial probability (Fig. 2). The Smart Explainer and Smart Predictor illustrate the explainable AI and smart prediction techniques used for the first time in the earthquake hazard assessment, respectively. All these combined choices were made because these AI techniques were never applied in earthquake probability and hazard estimation. The Smart Explainer and LIME explained the logic behind the obtained prediction results based on Smart Predictor based LightGBM. The flow of data points passes to Smart Predictor followed by encoders, LightGBM model, and Smart Explainer using the Shapash python library. Smart Predictor based prediction values for individual instances can be estimated. However, due to huge data points only the top five contributors for the probability assessment were derived. Finally, the importance, stability, interaction, contribution, and capacity towards the prediction were assessed. Secondly, an RNN model was developed for the prediction of spatial probability. Finally, the study implemented LIME where the explanations for RNN are considered trustworthy and a prediction report was extracted. The prediction results were then compared by producing spatial probability maps for both models. In the end, the earthquake hazard map was developed by using the spatial probability map with high accuracy and PGA.

4.1. PGA estimation

Several ground motion attenuation models are used to derive the PGA for 50 years for a 10% exceedance rate for the 475yrs return period.

(1) Data completeness analysis

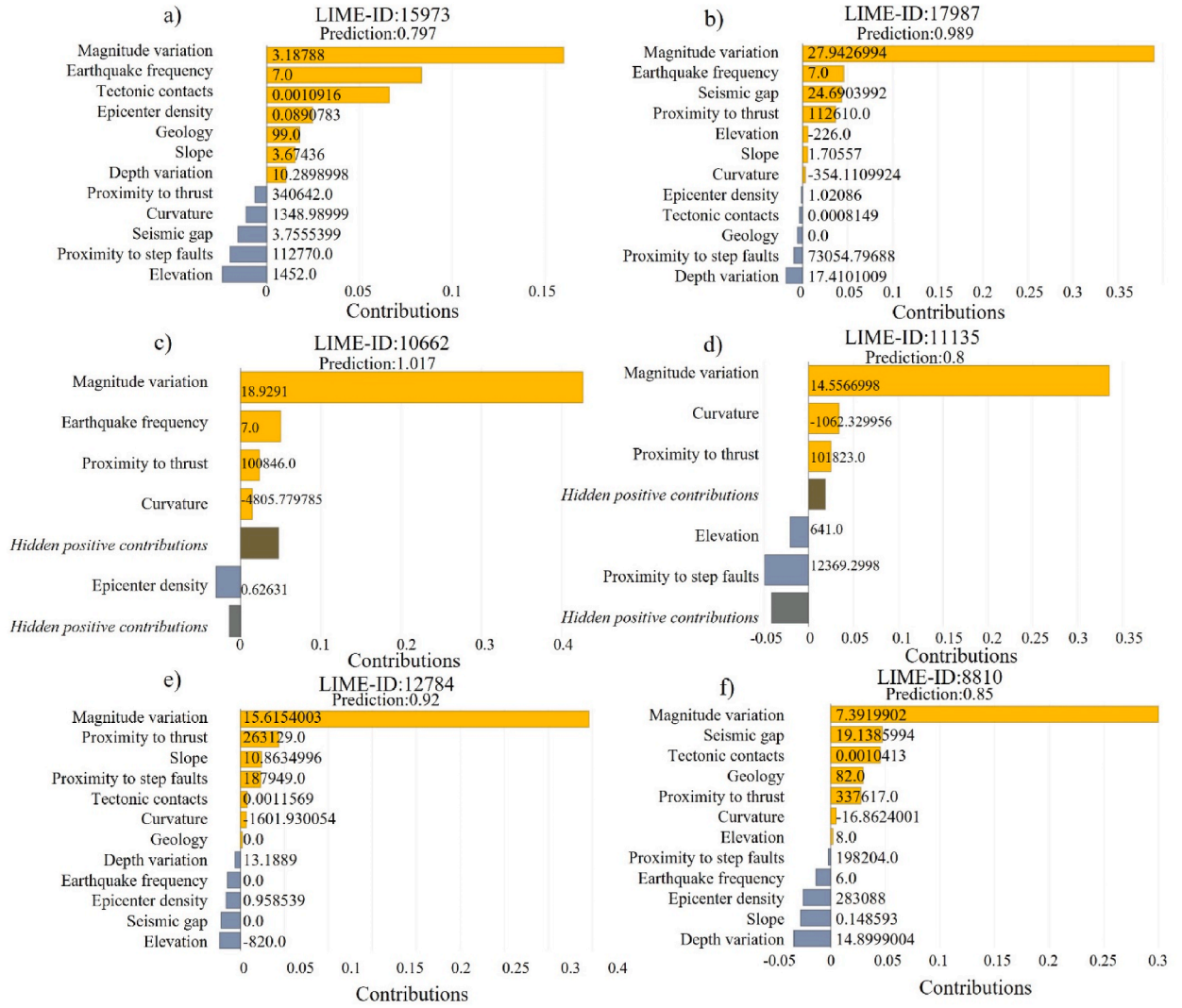

Fig. 6. Local explanation of factors based on the LIME model.

The overestimation or underestimation of earthquake parameters could occur due to the incompleteness of the events. The collected data is complete in a particular period of 1900–2023, the frequency of earthquakes for different magnitudes can be plotted against the calculated time from the last observation (Khan and Kalyan Kumar, 2018). Visual observation provides information regarding the completeness of data (Fig. 1(a)). Because data were collected from different sources which provide a constant slope therefore considered complete (Khan and Kalyan Kumar, 2018).

(2) Earthquake source modeling

Source modeling was performed where 0–50 km for shallow crustal faults and 50–175 km for subduction zones, and 175–300 km for deep earthquakes were considered. All the source categories were assembled through area sources characterized by a group of earthquakes. The earthquake parameters including observed magnitude, epicentral distance, source to site distance, faulting mechanism, tectonic environment, maximum magnitude range (Mmax), and ab-values are presented in Tables 2 and 3, respectively.

(3) Ground motion prediction attenuation function selection

The ground-motion prediction equation (GMPE) is a function of magnitude and source to site distance used to derive PGA that gives the ground motion value. The estimated ground motion value has a significant impact on the seismic hazard results. The earthquake mechanism was utilized to select the attenuation equation, epicenter distance and soil conditions (Icold 1989). In this study, the attenuation functions for Arabian Peninsula were described in Table 3.

(4) Seismic hazard estimation

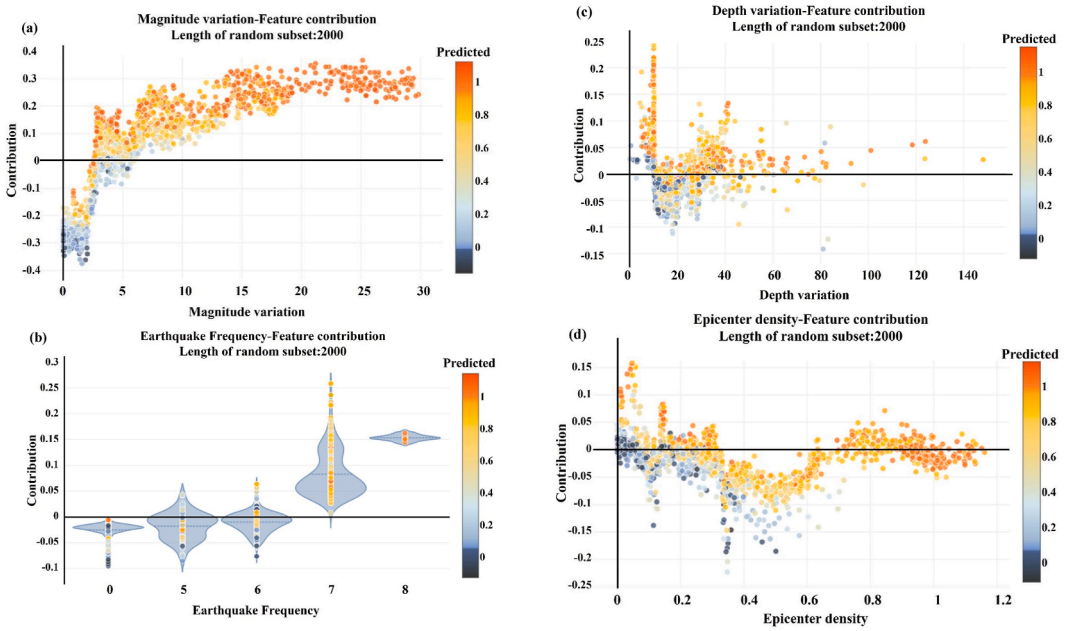

Fig. 7. The top four factors contribute to EHA based on Smart Predictor.

Peak ground acceleration was derived for Arabian Peninsula by covering the nearest subduction zone. The PGA values were derived for 50 years, equivalent to 475yrs return periods and multiplied with probability map to produce earthquake hazard map that demonstrates the PGA varies from 86 to 291 as high to very high hazard zones.

4.2. Data preprocessing and feature engineering

The study employed 12 thematic layers to implement the Smart Predictor based LightGBM model, and RNNs predictive model. The LightGBM model was explained using Smart Explainer and LIME backend whereas RNN was explained using LIME only. The earthquake data collected from USGS were trained along with randomly generated non-earthquake points by developing binary classification models. The detailed architecture and data flow of the employed models are shown in Fig. 3. The values of 12 indicators were extracted to numerical values in excel by keeping earthquakes and non-earthquake as the targets. Secondly, a Smart predictor based LightGBM model was developed for earthquake SPA where the model can continuously scan through several input indicators to classify earthquake (1) and non-earthquake (0) points. The supervised classifier was trained using 75% (training) and 25% (validation) on a random subset. For the training purposes, the dataset comprised of 30,000 samples were prepared for training and validation, respectively. The test datasets (2 million points) were used to estimate the SPA.

The Adam optimizer was utilized to optimize the model, and then batch size (100), validation split (0.25), and verbose (1) were implemented. A total of 123,002 trainable parameters were collected during the training. Thirdly, post-processing was conducted to convert the predicted values into pixels to generate the spatial probability map. To the end, the Smart Predictor predicted the top five local instances which were explained using Smart Explainer and LIME.

In the next step, an RNN model was developed for the binary supervised classification. Then the indicators were selected in a sequence to feed into the model by splitting the dataset into 75% (training) and 25% (validation). The layers were stacked and can be considered as single-band images. Using the Shapash library, factors were ranked based on importance. Depending on the importance, the series of layers feed the model as follows: magnitude variation, depth variation, tectonic contacts, seismic gap, earthquake frequency, epicenter density, elevation slope, proximity to step faults, proximity to thrust faults, curvature, and geology. Data were structured in descending order where each pixel value was converted within the sequence of significance. Consequently, the most and least important factors were sent first and last into the RNN model to process, respectively. Because of the RNN's recurrent structure, valuable information was retained and proceeded to the hidden layer. The Adam optimizer was implemented to optimize the RNN model, and then batch size (64), validation split (0.25), epoch (100), and loss function (0.001) were also utilized as RNN parameters. Thus, RNN proves to be a successful model for the prediction of the earthquake (1) and non-earthquake (0) targets that are later used for spatial probability mapping. Fig. 3 portrays the methodological workflow for the RNNs model.

4.3. Light gradient boosting machine

The light gradient boosting machine (LightGBM) is a framework that was developed based on boosting and decision tree (Ke et al., 2017). This model uses histogram-based algorithms for fast processing during the training period. The logic behind the histogram algorithm is to discretize eigenvalues into k bins that provide the idea of constructing a histogram with a width of k. Therefore, this algorithm does not require extra storage (Sun et al., 2020). The LightGBM model utilizes a maximum depth limit to prevent overfitting, ensuring high efficiency. The schematic diagram of the lightGBM model along with the factors and data flow, is shown in Fig. 3.

Table 4
The top five contributing factors and the prediction values towards earthquake SPA based on the Smart Predictor.

Row no (ID)	Smart Prediction	Factor 1	Value1	Contribution1	Factor 2	Value 2	Contribution 2	Factor 3	Value3	Contribution 3	Factor 4	Value4	Contribution 4	Factor 5	Value5	Contribution 5
1943	0.918835	Magnitude variation	6.94726	0.29896	Slope	7.28668	0.082885	Tectonic contacts	0.000861	0.019581	Earthquake frequency	0.0	−0.019516	Epicenter density	0.284445	0.014499
17987	0.988535	Magnitude variation	27.942699	0.390101	Earthquake frequency	7.0	0.045763	Seismic gap	24.690399	0.043516	Proximity to thrust	112610.0	0.036583	Depth variation	17.410101	−0.018553
3511	−0.000043	Magnitude variation	0.228586	−0.413192	Earthquake frequency	0.0	−0.028518	Epicenter density	0.0	0.023027	Proximity to step faults	1035330.0	−0.020926	Depth variation	13.7901	−0.020763
3353	0.007203	Magnitude variation	0.0	−0.405255	Elevation	835.0	−0.025753	Depth variation	13.5563	−0.019533	Earthquake frequency	0.0	−0.018402	Proximity to thrust	1681680.0	−0.017882
19930	0.037554	Magnitude variation	0.59493	−0.380052	Earthquake frequency	0.0	−0.02105	Depth variation	17.8358	−0.018491	Proximity to step faults	529812.0	−0.012416	Seismic gap	0.0	−0.010262

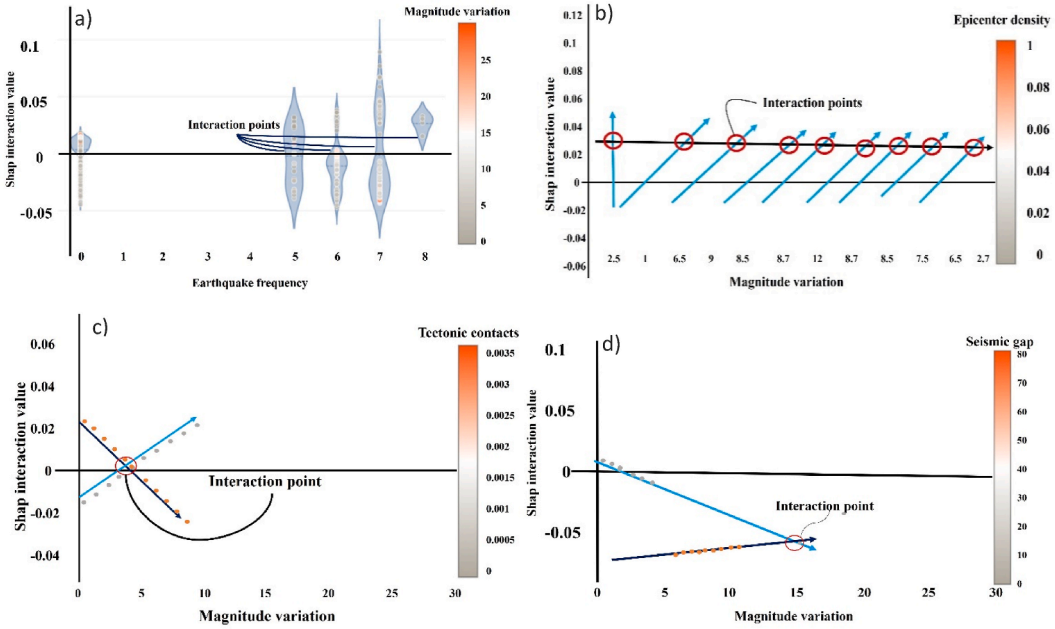

Fig. 8. Top four interaction values based on the Smart Predictor model. a) earthquake frequency vs. magnitude variation, b) magnitude variation vs. epicenter density, c) magnitude variation vs. tectonic contacts, d) magnitude variation vs. seismic gap. (Light blue arrow used for grey points and dark blue arrow used for red points). (For interpretation of the references to colour in this figure legend, the reader is referred to the Web version of this article.)

The detailed mathematical expression of LightGBM model is described as follows (Sun et al. 2020):

Given the training dataset $X = \{(x_i, y_i)\}_{i=1}^{m}$, LightGBM is focused to search for an approximation $\hat{f}(x)$ to the function $f^*(x)$ for minimizing loss functions values $L(y,f(x))$:

$$\hat{f}(x) \arg \min_{f} E_{y,x} L(y,f(x)) \tag{4}$$

LightGBM model can integrate numerous T regression trees $\sum_{t=1}^{T} f_t(x)$ for approximating the eventual model, presented as:

$$f_T(x) = \sum_{t=1}^{T} f_t(x) \tag{5}$$

The regression trees can be presented as wq(x),q ∈ 1,2, …,N, where N defines the tree leaves number, w is the leaf nodes sample weights and q is considered as the decision rule of trees. In the additive form, the model is trained where the step t can be described as follows:

$$\Gamma_t \cong \sum_{j=1}^{N} L\left(y_i, F_{t-1}(x_i) + F_t(x_i)\right) \tag{6}$$

The use of Newton's approach is used to approximate the objective function. Eq.(3) is modified when the constant term is removed:

$$\Gamma_t \cong \sum_{j=1}^{N} L\left(g_i F_t(x_i) + \frac{1}{2} h_i f_t^2(x_i)\right) \tag{7}$$

Where 1st- and 2nd-order gradient statistical results can be expressed by g_i and h_i of loss functions. The conversion of Eq. (4) can be done when the sample set of leaf j can be expressed by I_j:

$$\Gamma_t \cong \sum_{j=1}^{J} \left(\left(\sum_{i \in I_j} g_i \right) \omega_i + \frac{1}{2} \left(\sum_{i \in I_j} h_i + \lambda \right) \omega_j^2 \right) \tag{8}$$

where, the tree structure is q(x), ω_j^* is the optimum leaf weights and extreme values of Γ_T^* are defined by Eqs. (4) and (5):

Here, the quality of tree structure q(x) is measured by the weight function. The objective function can be obtained by split integration:

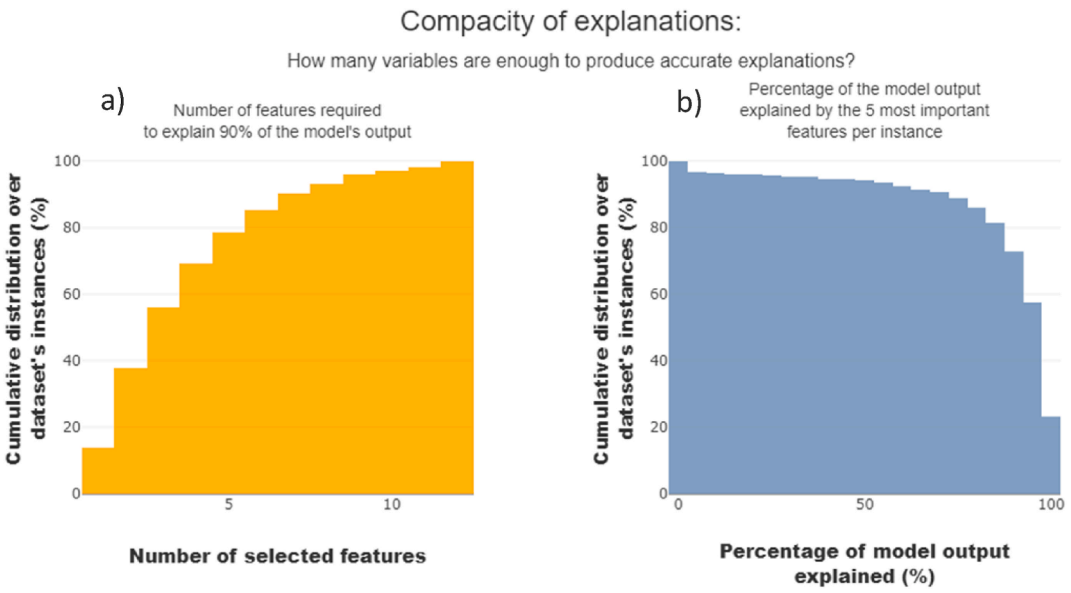

Fig. 9. Compacity and importance estimation of dataset instances for LightGBM model.

$$G = \frac{1}{2}\left[\frac{\left(\sum_{i\in I_l} g_i\right)^2}{\sum_{i\in I_l} h_i + \lambda} + \frac{\left(\sum_{i\in I_r} g_i\right)^2}{\sum_{i\in I_r} h_i + \lambda} + \frac{\left(\sum_{i\in I} g_i\right)^2}{\sum_{i\in I} h_i + \lambda}\right] \tag{9}$$

where, the left and right branch samples can be represented as I_l and I_r, respectively.

4.4. Recurrent neural network

A simple RNN model is characterized by input, hidden, and output layers. However, the model can process serialized data periodically by connecting to all nodes (Fig. 3). In comparison to other neural network models, RNNs process dynamic information in an orderly manner. In traditional neural networks, independent input and output values can be found. However, interaction among the nodes occurs in the hidden layer within the RNN model. Thus, the passing of information takes place within the network from one layer to another (Xu and Niu 2018).

The developed RNN model was constructed with a loopback. In the current work, the RNN model is made up of input as x_t , h_t as hidden, and the output can be denoted as y_t at time t. The mathematical expressions can be shown as follows (Jena et al., 2020a):

$$h_t = \sigma\left(W_h x_t + U_h h_{t-1} + b_h\right) \tag{10}$$

$$y_t = \sigma\left(W_y h_t + b_y\right) \tag{11}$$

where, W and U, are parameter matrices, σ(·) is denoted as the loss function of the training sequence, and b is the bias.

4.5. Local interpretable model-agnostic explanations

Given the black-box nature of the machine learning and deep learning models f, with a target value x to be explained (Fig. 3). The LIME model samples the black-box outcomes and near neighbors of x, and selects a model g out of the interpretable functional space G can be expressed as (Ribeiro et al., 2016);

$$\text{Argmin } g \in G^{L(f,g,\pi_x)+\Omega(g)} \tag{12}$$

Where the probability distribution can be defined as π_x around x and the penance is $\Omega(g)$ for the complexity of the model. Ribeiro et al. (2016) proposed numerous techniques to attain a sparse solution that includes K-LASSO as the explainable model. Generally, for K-LASSO, the penance is $\Omega = \infty\mathbb{I}\left[\left\|\omega_g\right\|_0 > K\right]$, where ω indicates sample points near x and the linear model coefficients to train K-LASSO. This process involves three uncertainty sources such as: i) Variation in sampling that explains a single row of data, ii) Parameters sensitivity, such as sampling size and proximity and iii) Explanation variance on the credibility of the model across data points.

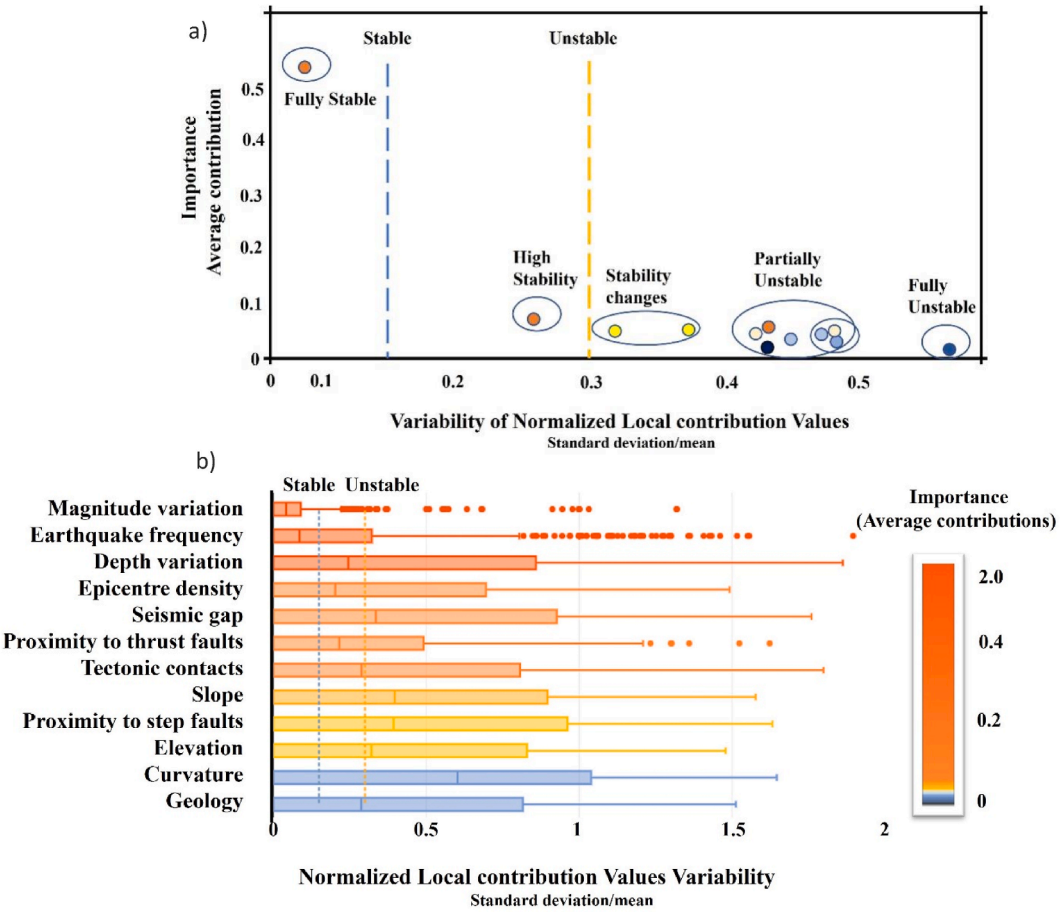

Fig. 10. Stability estimation of dataset instances for LightGBM model.

4.6. Smart Predictor and Smart Explainer

The Smart Predictor is the object that predicts the local instances by checking the consistency and contributions among the parameters. However, the Smart Explainer is the explanation object used to perform many operations to make the obtained outputs more understandable. The class of Smart Predictor is lighter than the Smart Explainer (https://www.maif.fr/). The Smart Predictor object has better prediction capacity with additional consistency inspection. The Smart Predictor utilizes the local explanation for the functional requirements. The end users can switch from data mining models to Smart Predictor objects. The current study switches from Smart Explainer to Smart Predictor using Shapash codes, which help in reproducing the prediction results with the right structure (Fig. 3). The parameter consistency can be checked using the Smart Predictor. The object class applies preprocessing, post-processing estimates model contributions and predictions and abides by local explainability. The Smart Predictor allows end users to customize the summary for their use. The Smart Predictor can be implemented in batch mode or API. The steps include building, saving, and loading a Smart Predictor – adding input – using labels– outlining an explanation for the Smart Prediction of instances.

4.7. Evaluation metrics

The study uses 12 factors that include seismological, geological, and geo-structural as conditioning factors (Table 1). The statistical metrics that were used to assess the predictive capacity are as follows: recall (TPR), F_1-score (F_1), precision (PPV), support and accuracy (ACC) (Jena et al., 2020a,b). The mathematical expression of these metrics is shown in Equation (7)-10.

$$TPR = \frac{TP}{P} = \frac{TP}{TP + FN} = 1 - FNR. \tag{13}$$

$$F_1 = 2 \times \frac{PPV \times TPR}{PPV + TPR} = \frac{2TP}{2TP + FP + FN}. \tag{14}$$

where, TPR stands for true positive rate or hit rate whereas F_1-score is the harmonic mean of precision and sensitivity. The precision and accuracy can be represented as:

$$PPV = \frac{TP}{TP + FP}. \tag{15}$$

$$ACC = \frac{TP + TN}{P + N}. \tag{16}$$

where, PPV stands for positive predictive value and ACC denotes accuracy. Here, N and P denote negative and positive datapoints points where TP is true positive, FP as false positive and TN stand for true negative, respectively.

5. Results

5.1. Local interpretable explanation for LightGBM

The study shows the results of LIME interpretation to interpret the black-box models (Light Gradient Boosting) trained with 12-factors for earthquake and non-earthquake prediction. Given that the LIME model runs on a subset of rows of data points, we observed that various importance of factors because of sampling variance. The highest importance is achieved by magnitude variation and earthquake frequency. Fig. 4(a) demonstrates the factors' importance in SPA.

5.1.1. Local importance of factors

The earthquake dataset has been chosen for this study, which needs highly non-linear models for the correct evaluation of the probability of two classes for each instance. Fig. 4(b) shows LIME explanations obtained for 17 instances, making a subset for the LightGBM model. The 17 highly contributing instances in magnitude variation and tectonic contacts show higher importance than global importance. The highest importance was attained by magnitude variation (0.65), and earthquake frequency (0.07) while the lowest was by geology (0.01). According to the LIME explanations, the top four important factors are magnitude variation, earthquake frequency, depth variations, and epicenter density.

5.1.2. Global importance of factors

In this study, A total of 3000 instances were chosen to obtain an overall knowledge of global importance as compared to local importance. The 17 instances made a subset portrays that the two factors such as magnitude variation and earthquake frequency have high global importance, thus confirming their stability (Fig. 4(b)). Fig. 5 shows the differences in the local and global importance of factors, which may influence the stability of the model. According to Fig. 4(b), the global importance of magnitude variation is lower as compared to local importance. In the case of earthquake frequency, the global importance is higher than the local importance. Similarly, for other factors, the observed uncertain importance in Fig. 4(b) can maintain the subset importance to achieve good prediction output. Spatial correlation among the emerged factors such as magnitude variation vs earthquake frequency (0.21), magnitude variation vs depth variation (0.22), magnitude variation vs epicenter density (0.93) and earthquake frequency vs epicenter density (0.18) make the topmost important factors for SPA.

5.1.3. LIME for individual instances in LightGBM

The LIME explanations are sparse with high interpretability. Since the tabular data is used in this study, a tabular explainer object was implemented through the LIME model. This object explainer can explain the model prediction for individual rows in the test data set. The specific rows are mostly contributing to the earthquake prediction, as shown in Fig. 6. The graphs convey why these rows are predicting earthquakes instead of non-earthquake. Because the topmost important factors such as magnitude variation, earthquake frequency, epicenter density and tectonic contacts are contributing more towards earthquake prediction. Local explanations for sample numbers 10662 and 11135, the hidden contributions towards the earthquake and non-earthquake prediction were shown in Fig. 6 (c)–(d). For sample number 10662, the hidden contribution is more toward earthquake, while in the case of sample 11135, the contribution is more toward non-earthquake prediction. All the local explanations presented show the individual prediction values.

The values in orange are the main reason for the final prediction, whereas values in light blue are ignored. In Fig. 6, the sample numbers 15973,17987, 12784, and 8810 show a 100% probability of the earthquake samples. In the first sample, 15973, the factors with high magnitudes, high frequency, and tectonic contacts contribute to the prediction. The LIME model has rightly predicted the targeted point as an earthquake. The prediction result (0.797) that is above 0.5 makes sense in our mental model. Earthquake probability is mostly characterized by magnitude variation, epicenter density and frequency have a very high likelihood of predicting an earthquake. The decision has been made based on the factors in the case of sample number 17987. The fact characteristics such as depth variation, tectonic contacts, geology, and step faults have tried to pull down the likelihood of an earthquake, but overall, the model determined with the result (0.989) that shows the prediction is an earthquake point.

5.2. Feature contribution based on Smart Predictor and Smart Explainer

A factor's importance could be determined by how it contributed to the prediction of an adopted model. Fig. 7 shows the contribution of each factor during the development phase of the Smart Predictor-based lightGBM model. These contribution values are obtained using the Smart Explainer model for each trial when Smart Explainer interprets a Smart Predictor-based lightGBM model. The Smart Explainer model apprehends the signal of the top four factors, which are globally used for the SPA. The top four factors were magnitude variation, earthquake frequency, depth variation, and epicenter density according to the factors' contribution. Fig. 7(a-d) demonstrate the highest contribution towards SPA. The red data points in Fig. 7 denote a high contribution that predicts earthquakes

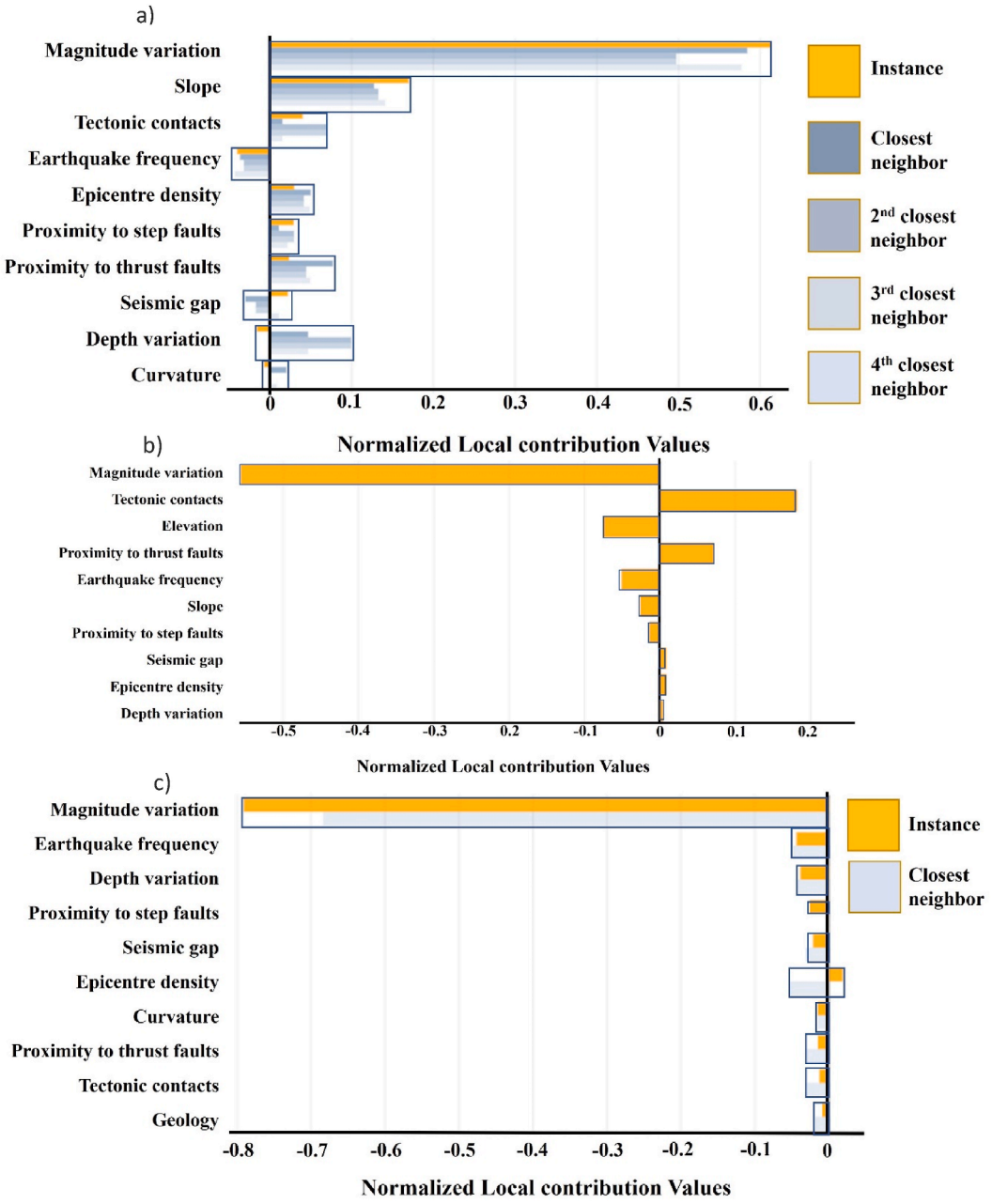

Fig. 11. Comparing local explanations in neighborhoods for specific rows of the dataset.

while dark blue predicts non-earthquakes. In a few cases, low/negative contribution values predict earthquakes, whereas high/positive contribution values predict non-earthquakes.

By default, it can be noticed that the Smart Explainer draws 2000 samples (38% of total data) from a standard normal distribution from the test data. Here, the training variance is the one that estimates the sampling proximity. The Smart Explainer model better captures the locally influential factors with smaller sampling proximity that picks up global factors with larger proximity. The Smart Explainer model explores both local and global data structures. The top four contributions, factor values, and prediction values calculated using Smart Predictor are presented in Table 4.

5.2.1. Factors' interaction

Factors' interaction during prediction can be understood using interaction plots obtained by Smart Predictor. To analyze the prediction model, the influence of combinations of factors on the output was assessed. Shapash library permits quick scrutiny of the model by showing the factors that have the highest possibility of achieving the interactions of the factors (https://github.com/MAIF/shapash). We observed the top four interactions towards the earthquake probability. The top four factors' interactions contribute the

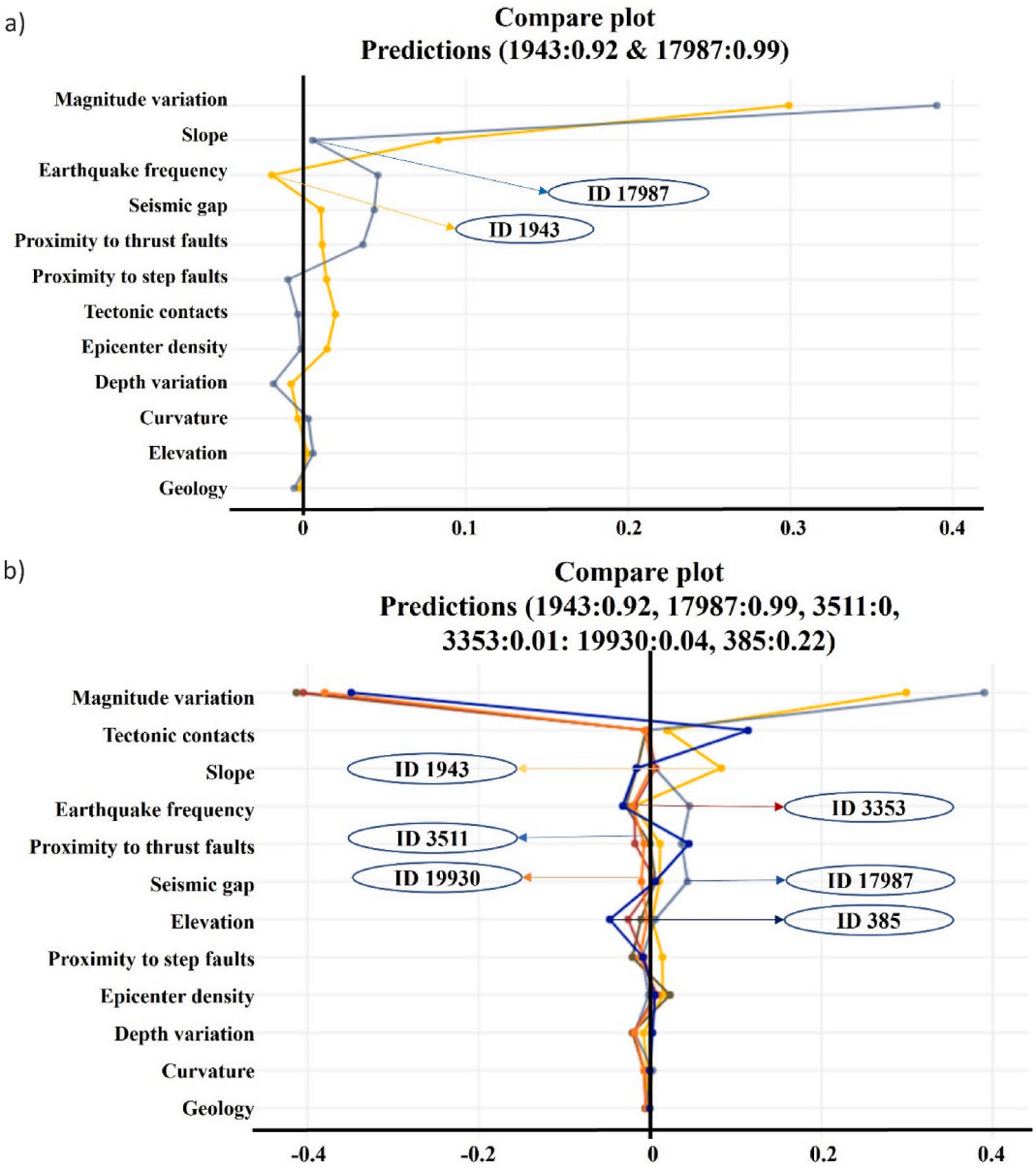

Fig. 12. Comparing local explanations in neighborhoods for specific rows of the dataset using a line graph to better compare the prediction outputs with LIME.

highest towards earthquake prediction compared to non-earthquake probability. Fig. 8(a-d) depicts four interactions including, earthquake frequency versus magnitude variation, magnitude variation versus epicenter density, magnitude variation versus tectonic contacts and magnitude variation versus seismic gap. In the first case, the highest interaction values associated with high earthquake frequency with the highest magnitude predict an earthquake. Similarly, Fig. 8b and c shows positive and mixed interaction values in association with epicenter density and high tectonic contacts, and Fig. 8(d) depicts high magnitude variation with the highest seismic gap areas that are prone to high earthquake probability, respectively.

5.2.2. Compacity, importance and stability explanations

This study measured the influence of the sum of important contributions on the model's global decision. Two graphs have been presented that portray the link among a required number of factors, their approximation level, and the dataset proportion (Fig. 9). The orange bars in Fig. 9(a) show that the top 5 factors reach the default approximation for 79% of the instances; however, all the factors are required to explain 90% of the model's output. Thus, for accurate explanations, a subset of factors could generate a reliable explanation for the largest portion of instances. The top 5 factors in Fig. 9(b) reached up to 80% of the lightGBM model for 80% of the cases. Thus, all factors should be included in the explanations for extremely precise outputs. Stability can be expressed when similar explanations can be observed in a very similar fashion.

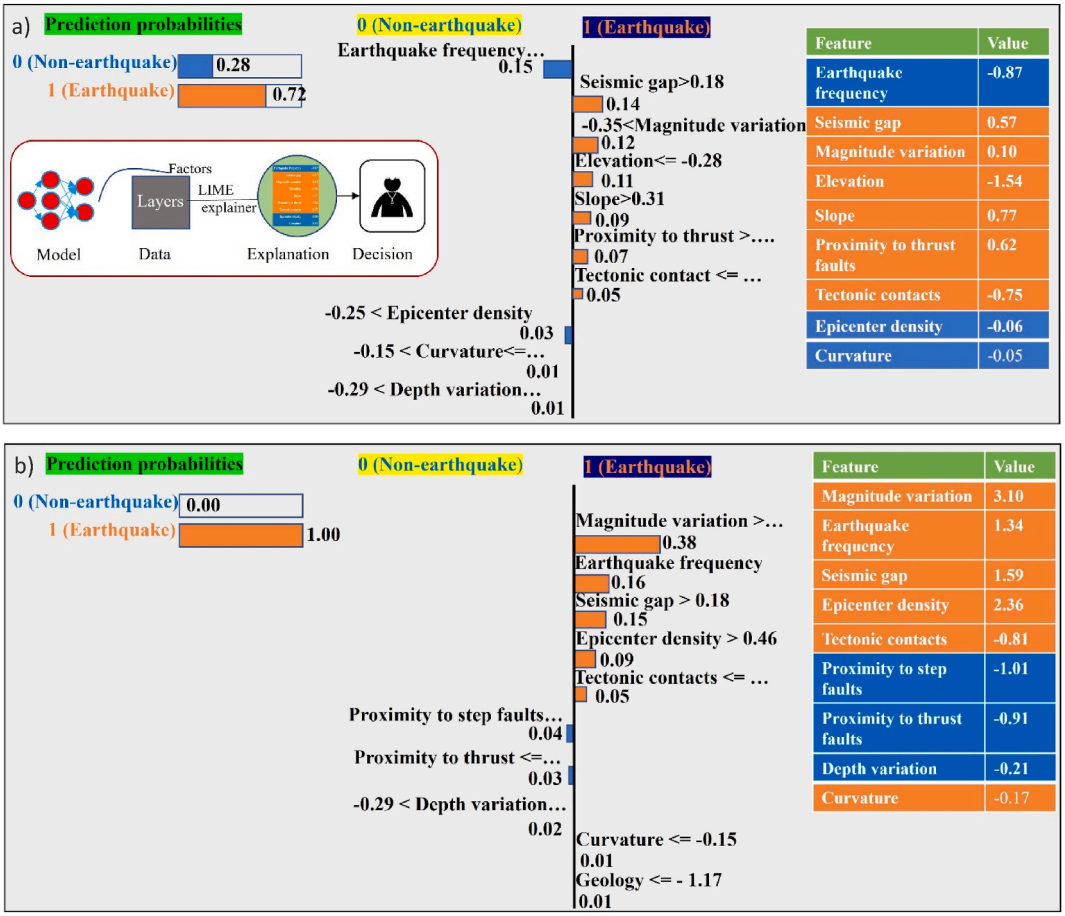

Fig. 13. LIME explanation for sample numbers of a) 1943, and b) 17987 based on RNN.

The instances similarity was evaluated using two criteria including the closeness of instances in factors space and the similarity between the outputs. Fig. 10(a) demonstrates the neighborhood around every instance. The y-axis shows the average factor's importance depending on their contributions throughout the data. The x-axis represents the variability of the average contribution of factors throughout the instances' neighborhood. Therefore, left factors such as magnitude variation, and earthquake frequency are stable in the neighborhood, unlike other factors on the right (Fig. 10(a)). In Fig. 10(b), magnitude variation and earthquake frequency seem to be strong and relatively stable, boosting the confidence in using them for explanations. Similarly, all other 10 factors are unstable, making us careful before using these factors for explanations. Therefore, a comparison of local explanations in a neighborhood can be displayed and explained as shown in Fig. 11.

In the case of neighborhood comparison, it is difficult to interpret the factors contributing to the output. The sample numbers 1943 and 17987 (Fig. 12(a)) show a similar trend in terms of contribution to probability assessment. Fig. 12(b) shows how completely opposite suggestions could be observed for samples such as 3511, 3353, 19930 and 385 in the same neighborhood. The low similar contribution trends are estimating non-earthquake probability, while high contributing trends are evaluating earthquake probability.

5.3. Local interpretable explanation for RNN

A tabular explainer object was created using the LIME library to explain the model output. The expectation is to interpret a single observation from the test data. The LIME model was implemented for the sample numbers 1943 (Fig. 13a) and 17987 (Fig. 13b) of data projecting the highest contribution towards the earthquake spatial probability. The model is 72% confident for the 1943rd row, which is an earthquake point. The values of the seismic gap, magnitude variation, elevation, slope, proximity to thrust, and tectonic contacts increase the probability of being classified as an earthquake. The epicenter density, curvature, and depth variation are the ones that decrease the earthquake probability.

In the case of the 17987th row of test data, the model is 100% confident that the point is an earthquake point, and the top three predictors are magnitude variation, earthquake frequency, and seismic gap. This is how LIME works for an RNN model in a nutshell. A variety of visualizations are available, and this is not limited to interpreting instances individually, but this is the best way to understand the prediction individually.

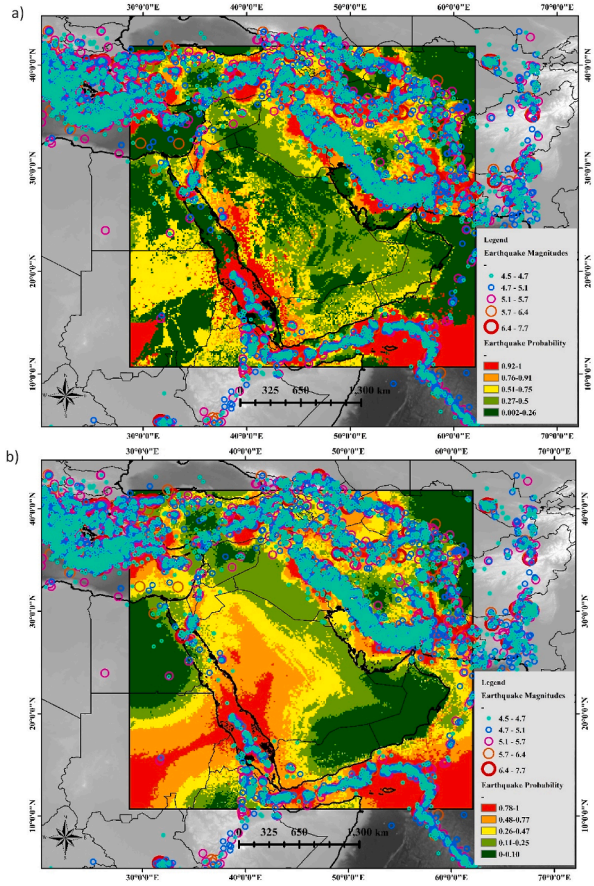

Fig. 14. Spatial probability maps: a) with, and b) without stable factors for the LightGBM model and Smart Predictor.

5.4. Spatial probability and hazard index estimation

The earthquake SPA was estimated using machine learning (LightGBM) and deep learning (RNN). Finally, the hazard was estimated by considering the peak ground velocity and spatial probability. However, the earthquake and non-earthquake points were predicted using the above-mentioned models. According to the LightGBM results, the probability areas were classified into five classes: very-high (0.92–1), high (0.76–0.91), moderate (0.51–0.75), low (0.27–0.5), and very-low (0.002–0.26). Similarly, based on the RNN results, the probability areas are very-high (0.79–1), high (0.57–0.78), moderate (0.36–0.56), low (0.17–0.35) and very-low (0–0.16). According to the model results, the Zagros zone with high seismic probability is located outside of the Arabian Peninsula. The highly probable areas in the Arabian Peninsula could be distributed across the Gulf of Aqaba–Dead Sea, Red Sea, Gulf of Aden, and Zagros fault zone in Iran. In comparison to the exception of high probable areas, major parts of the Arabian Peninsula show relatively low spatial probability. According to the hazard map, the PGA in the Arabian Peninsula varies between 15 cm/s^2 and 291 cm/s^2 for the 475y return period. Relatively high seismic hazards could be found in Yemen, Northern Syria, and the Iraq–Iran border, Anatolian fault region of Turkey. This shows similar results to the published maps (Al-Haddad et al., 1992, 1994), where the PGA values reach up to 50 cm/s^2. This delineates that the peninsula is threatened due to major active structures along the Arabian Plate border. Thus, the current seismic hazard maps contemplate the standard seismotectonic setting of the Peninsula. Fig. 14(a) shows the spatial probability with all the important factors, whereas 14(b) shows the map without stable factors such as magnitude variation and earthquake frequency based on the LightGBM model. According to the RNN model, spatial probability in Fig. 15(a) shows similar results with LightGBM in Fig. 14(a). However, the results completely changed without the stable factors as shown in Fig. 15(b). The accuracy of LightGBM (89%) and RNN (87%) models was described in Table 5, which confirms that Smart Predictor-based LightGBM provides better output than RNN. Because of the high accuracy, the LightGBM model was chosen for hazard estimation as shown in Fig. 16. The highest PGA values can be observed from a 2 km depth to 2 km of elevation whereas, the high PGA values vary between 0 and 20° in and around Arabian Peninsula, which is evident in Fig. 16(a).

6. Discussion

The current study demonstrates the probability of futuristic earthquakes that could occur in the mapped spatial probability zones. Seismic quiescence could be observed in the Makran Subduction Zone and the Gulf of Aqaba, which are falling under the seismic gap. This confirms that further study is required on tectonics, spatial probability, and hazard in the Arabian Peninsula. The inventory map

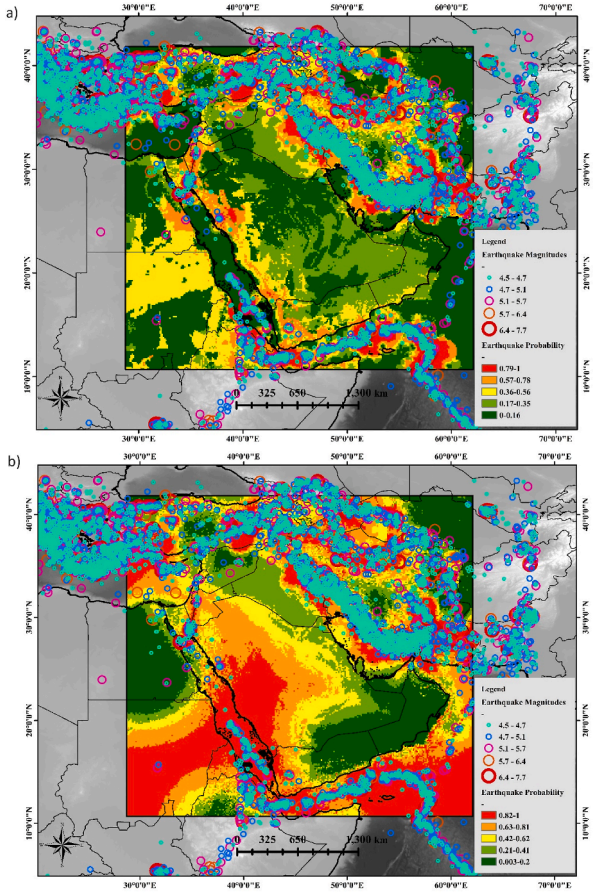

Fig. 15. Spatial probability maps: a) with, and b) without stable factors for the RNN model.

Table 5
RNN and LightGBM prediction accuracy report.

RNN report		Precision	Recall	F1-score	Support
	Non-earthquake	0.8990	0.8248	0.8603	3162
	Earthquake	0.8359	0.9059	0.8695	3114
	Accuracy			0.8650	6276
	Macro average	0.8674	0.8654	0.8649	6276
	Weighted average	0.8677	0.8650	0.8649	6276
	Prediction accuracy: 0.87				
LightGBM report		Precision	Recall	F1-score	Support
	Non-earthquake	0.91	0.87	0.89	3423
	Earthquake	0.88	0.92	0.90	3481
	Accuracy			0.89	6904
	Macro average	0.90	0.89	0.89	6904
	Weighted average	0.90	0.89	0.89	6904
	Prediction accuracy: 0.89				

suggests that the strong ground shaking at Najran, Sohar, Nizwa, Qalhat, Makah, Al-Madinah, Taief, and Tabuk demonstrate the seismic hazard warnings. Nevertheless, the recorded events suggest that the Arabian Peninsula is aseismic in nature (Al-Haddad et al., 1994; Al-Shijbi et al., 2019). The spatial probability is tied to Iran and Turkey faults and all the Gulfs surrounding the Peninsula indicate a localized hazard.

This research applied 13 factors with the aim of spatial probability and hazard analysis, with a clear vision of model interpretability using explainable AI. The results achieved by LightGBM-based Smart Predictor, and Smart Explainer were compared with the LIME-based RNN results for a return period of 475 years. The findings of the current work are consistent with Al-Haddad et al. (1994) which show similar spatial outputs. This study estimated SPA based on binary machine and deep learning prediction techniques, representing 0 (non-earthquake) and 1 (earthquake) as the probability values. The Smart Predictor predicted the earthquake and non-earthquake points with minimal error and the outputs were explained using Smart Explainer and LIME. Smart Predictor shows a prediction report for each individual prediction. However, the top five prediction results are shown in Table 4.

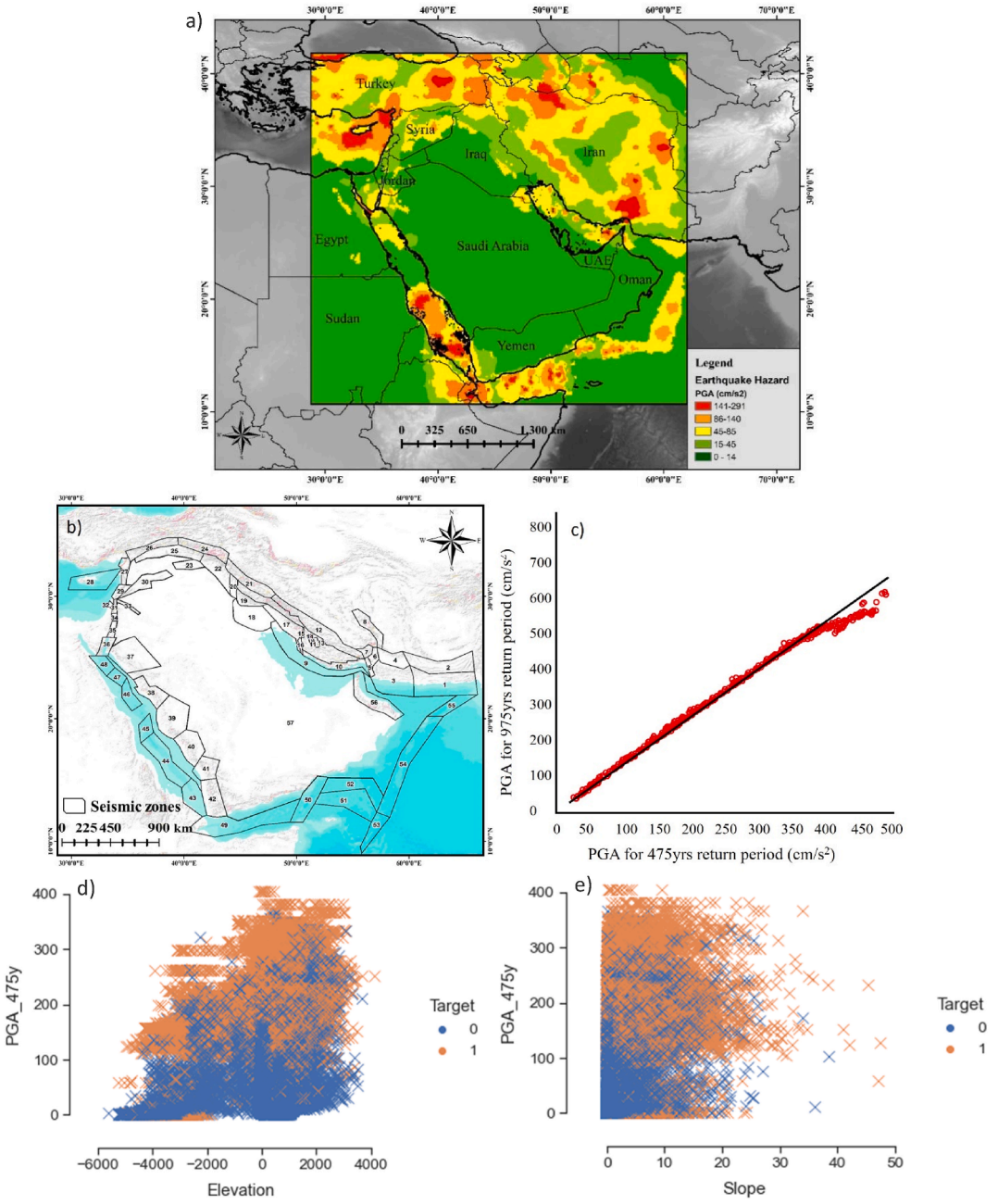

Fig. 16. a) Earthquake hazard map for Smart Predictor-based LightGBM model. c) Seismogenic zone in Arabian Peninsula (Modified from Al-Shijbi et al., 2019), d) PGA475yrs vs PGA975 yrs, d) PGA in Arabian Peninsula with respect to Elevation, and e) Slope.

According to Smart Predictor, the top five important factors are magnitude variation, earthquake frequency, depth variation, epicenter density, and seismic gap. However, the top contributing rows worth of data were explained using LIME which shows the prediction values reached above 0.5 directing towards earthquake while below 0.5 indicates non-earthquake areas. The top four factors' interaction is presented in Fig. 8, demonstrating how the important factors interact to achieve excellent output. In the case of RNN, the prediction was conducted with excellent accuracy and the outputs were explained using LIME. The LIME model explained two individual rows of test sets with their contribution to probability estimation. The results demonstrate the reasons for the excellent prediction values. This suggests that Smart Predictor performs better output than RNN-based probability. Currently, Smart Predictor is not linked to deep learning, thus in its nascent stage. Smart Predictor and Smart Explainer involvement with deep learning in the future might improve accuracy. The LIME results of the LightGBM model were compared to the LIME results of RNN for sample numbers 1943 and 17987 (top contributors).

According to the LIME explanation, the prediction results for both the sample numbers are 0.92 and 0.99 (LightGBM) and 0.72 and 1.0 (RNN) models, respectively. This shows that the outputs are similar with minor changes, making the prediction outputs trustable for spatial mapping. For both the models of LIME explainability, the stable factors are earthquake frequency and magnitude variation which can be confirmed through the stability explanations in Fig. 10. According to the nearest neighbor comparison, as shown in Fig. 11, the normalized contribution of instances was compared with their neighbors for sample numbers 1943, 385 and 19930. It is evident that the common factors that show the highest normalized contribution in all instances are earthquake frequency and magnitude variation, which is similar in other neighbors, however making the values shaky for other factors. The obtained maps were again compared with (excellent results) and without the important factors (poor results) for both the models that show spatial variance. No deep learning-based studies could be found for the comparison in this study area for spatial probability and hazard assessment. Therefore, the spatial probability maps obtained based on LightGBM and RNN with important factors were compared, showing a better map obtained using Smart Predictor than the simple RNN model-based spatial outputs. However, the obtained hazard map (PGA varies 15 cm/s^2 to 291 cm/s^2 in Arabian Peninsula) is consistent with previous maps to a great extent, with the PGA values 250 cm/s^2 as derived by Al-Haddad et al. (1994) in the southwestern part of Saudi Arabia. The differences that could be observed in the maps might be due to (1) updated catalog and recent GMPEs implementation, (2) involvement of all the seismic sources, (3) first-time use of Smart Predictor, Smart Explainer and LIME, and (4) use of both machine learning and deep learning techniques. The central portion of Saudi Arabia, Egypt, and Sudan falls in low-hazard zones. Medium-to-high hazards could be found in coastal regions of the Arabian Peninsula. Gulf areas, areas close to the Red Sea, Iran and Turkey are coming under very-high hazard zones. Therefore, this study may convey the improved version of seismic hazard analysis using the Smart Predictor-based LightGBM model as shown in (Fig. 16). Jena et al. (2020) conducted a study on earthquake probability, hazard and risk assessment using convolutional neural networks and achieved an accuracy of 89.47%. Gitis and Derendyaev (2019) applied machine learning models for seismic hazard forecasts and illustrated good seismic zoning for active seismic zones. Alizadeh et al. (2018) conducted a study for earthquake vulnerability assessment using ANN with an accuracy of 95.66%. Silva-Lopez et al. (2022) implemented a deep learning model with 97% accuracy for seismic risk assessment and explained using XAI. In comparison to the above-mentioned models, the accuracy of the currently applied machine learning models provides good accuracy in association with all factors. The limitations of Smart Explainer deal with only gradient boosting models whereas LIME deals with several ML models. LIME is unstable and depends on random sampling whereas SHAP can be implemented in conjunction with LIME for better understanding (Amin et al., 2022). LIME generates an explanation for a subset of total data, while SHAP requires the entire dataset to calculate SHAP values. The major challenge is to analyze multivariate earthquake hazards due to the influence of various factors such as uncertainty, training procedures and input variables in the modelling process.

7. Conclusions

In this study, a Smart Predictor, Smart Explainer, and LIME were used for the LightGBM model, whereas only the LIME explainer was used for the RNN model to produce the earthquake spatial probability map in the Arabian Peninsula. This work is limited to hazard estimation followed by spatial probability using ML-based smart applications and deep learning. The models used 12 factors to distinguish the earthquake and non-earthquake points. Prediction results were explained, where Smart Predictor-based LightGBM provides better spatial outputs than the RNN model. Based on the LIME probability, the stable factors (magnitude variation, earthquake frequency), important factors (magnitude variation, earthquake frequency, depth variation, epicenter density and seismic gap) and irrelevant factors were identified. Global stability was explained using Smart Explainer-based LightGBM and local stability was explained using LIME. Redundant factors were removed to improve the model performance and the top five interactions can quickly explain the spatial probability outputs. A comparative assessment was conducted between the LightGBM and RNN model outputs. Both LIME and Smart Explainer prove to explain the outputs with excellent reasons. In addition, the Smart Explainer can provide a report on the explanation, making the LightGBM to be an outstanding prediction model for earthquake spatial probability assessment. The LightGBM model achieved an overall accuracy of 89%, whereas RNN achieved 87% with all features. According to the results, the Gulf of Aden, Red Sea, Iran, and Turkey are falling under a very-high spatial probability index (0.991–1). Similarly, Gulf areas, areas close to the Red Sea, areas in the Zagros fault and Anatolian fault zone are coming under very-high hazard zones. For better accuracy, a vast training dataset should be created because the AI industry is shifting from model-centric to data-centric. The current challenges to creating vast datasets for AI model training include data scarcity, privacy, and security. Moreover, new explainable AI can be used to detect the limitations such as interpretability and reproducibility. To this end, Smart Predictor, Smart Explainer, LIME, and selection of machine and deep learning models enable us to analyze and guide in detail on spatial probability and hazard estimation. The major application of the XAI is to interpret and explain the machine learning models and their results. To sum up, applied XAI models enable algorithmic transparency, actionability, satisfaction, selection/simplicity, predictability, and robustness in SPA mapping. Future developments of deep learning-based Smart Predictor are in the nascent stage, which will no doubt improve the SPA and EHA. These Smart Predictor-based AI models could bring a change to geological/seismological research in the future.

Author contributions

“Conceptualization, R.J., A.S., and R.A.R.; Methodology, R.J., A.S., R.A.R., M.B.A.G., O.G; Software, R.J.; Validation, R.J., A.S., R.A.R.; Formal Analysis, R.J., A.S., R.A.R., O.G; Investigation, R.J.; Resources, R.J.; Data Curation, R.J.; Writing-Original Draft Preparation, R.J.; Writing-Review & Editing, A.S., R.A.R., B.P., M.B.A.G., O.G., M.A.K., and P.G.; Visualization, R.J., A.S., R.A.R., B.P., M.B.A.G.; Supervision, A.S.; R.A.R.; Project Administration, R.A.R., and A.S.; Funding Acquisition, A.S., R.A.R., P.G. and O.G. “All authors have read and agreed to the published version of the manuscript.”

Declaration of competing interest

The authors declare that they have no known competing financial interests or personal relationships that could have appeared to influence the work reported in this paper.

Data availability

Data will be made available on request.

Acknowledgments

The work was supported by the GIS and Remote Sensing Center, Research Institute of Sciences and Engineering, University of Sharjah, UAE through the Vice Chancellor Research Fund and the APC was funded by the Institute of Advanced Research in Artificial Intelligence (IARAI) GmbH, Vienna, Austria. The authors would like to thank the anonymous reviewers for their valuable suggestions to improve the manuscript.

References

Abdalla, J.A., Al-Homoud, A., 2004,. Earthquake hazard zonation of eastern Arabia. In: In13th World Conference on Ear*thquake Engineering*. Canada, Vancouver, BC.
Abdollahi, A., Pradhan, B., 2021. Urban vegetation mapping from aerial imagery using explainable AI (XAI). Sensors 21 (14), 4738.
Abdollahi, A., Pradhan, B., 2023. Explainable Artificial Intelligence (XAI) for Interpreting the Contributing Factors Feed into the Wildfire Susceptibility Prediction Model, vol. 879. Science of The Total Environment, 163004.
Adeli, H., Panakkat, A., 2009. A probabilistic neural network for earthquake magnitude prediction. Neural Network. 22 (7), 1018–1024.
Akkar, S., Bommer, J.J., 2010. Empirical equations for the prediction of PGA, PGV, and spectral accelerations in Europe, the Mediterranean region, and the Middle East. Seismol Res. Lett. 81 (2), 195–206.
Al-Amri, A.M., 1995. Recent seismic activity in the northern Red Sea. J. Geodyn. 20 (3), 243–253.
Al-Amri, A.M., 1998. Earthquakes Data Base of the Arabian Peninsula. SSC – Technical Report. Seismic Studies Center. King Saud University, pp. 1–11.
Al-Dogom, D., Al-Ruzouq, R., Kalantar, B., Schuckman, K., Al-Mansoori, S., Mukherjee, S., Al-Ahmad, H., Ueda, N., 2021. Geospatial multicriteria analysis for earthquake risk assessment: case study of Fujairah City in the UAE. J. Sens. 2021, 1–25.
Al-Haddad, M., Siddiqi, G.H., Al-Zaid, R., Arafah, A., Necioglı, A., Turkelli, N., 1992. Seismic hazard and design criteria for Saudi Arabia. Proc. of 10th WCEE 449–454.
Al-Haddad, M., Siddiqi, G.H., Al-Zaid, R., Arafah, A., Necioglu, A., Turkelli, N., 1994. A basis for evaluation of seismic hazard and design criteria for Saudi Arabia. Earthq. Spectra 10 (2), 231–258.
Al-shijbi, Y., El-Hussain, I., Deif, A., Al-Kalbani, A., Mohamed, A.M., 2019. Probabilistic seismic hazard assessment for the Arabian Peninsula. Pure Appl. Geophys. 176, 1503–1530.
Alarifi, A.S., Alarifi, N.S., Al-Humidan, S., 2012. Earthquakes magnitude predication using artificial neural network in northern Red Sea area. J. King Saud Univ. Sci. 24 (4), 301–313.
Aldama-Bustos, G., Bommer, J.J., Fenton, C.H., Stafford, P.J., 2009. Probabilistic seismic hazard analysis for rock sites in the cities of Abu Dhabi, Dubai and Ra's Al Khaymah, United Arab Emirates. Georisk 3 (1), 1–29.
Alizadeh, M., Alizadeh, E., Asadollahpour Kotenaee, S., Shahabi, H., Beiranvand Pour, A., Panahi, M., Bin Ahmad, B., Saro, L., 2018. Social vulnerability assessment using artificial neural network (ANN) model for earthquake hazard in Tabriz city, Iran. Sustainability 10 (10), 3376.
Allahvirdiasl, H., Shahabi, H., Mohammadi, A., Shirzadi, A., Chen, W., Ahmadi, M., Khodadadi, M., 2022. Evaluation of geo-hazard induced by Zarand earthquake in Central Iran using thermal remote sensing data and GIS. In: In*Environmental Degradation in Asia: Land Degradation, Environmental Contamination, and Human Activities*. Springer International Publishing, Cham, pp. 69–87.
Amin, M.N., Salami, B.A., Zahid, M., Iqbal, M., Khan, K., Abu-Arab, A.M., Alabdullah, A.A., Jalal, F.E., 2022. Investigating the bond strength of FRP laminates with concrete using LIGHT GBM and SHAPASH analysis. Polymers 14 (21), 4717.
Ambraseys, N.N., Simpson, K.U., Bommer, J.J., 1996. Prediction of horizontal response spectra in Europe. Earthq. Eng. Struct. Dynam. 25 (4), 371–400.
Asim, K.M., Martínez-Álvarez, F., Basit, A., Iqbal, T., 2017. Earthquake magnitude prediction in Hindukush region using machine learning techniques. Nat. Hazards 85, 471–486.
Atkinson, G.M., Boore, D.M., 2003. Empirical ground-motion relations for subduction-zone earthquakes and their application to Cascadia and other regions. Bull. Seismol. Soc. Am. 93 (4), 1703–1729.
Atkinson, G.M., Boore, D.M., 2006. Earthquake ground-motion prediction equations for eastern North America. Bull. Seismol. Soc. Am. 96 (6), 2181–2205.
Beroza, G.C., Segou, M., Mostafa Mousavi, S., 2021. Machine learning and earthquake forecasting—next steps. Nat. Commun. 12 (1), 4761.
Campbell, K.W., 2003. Prediction of strong ground motion using the hybrid empirical method and its use in the development of ground-motion (attenuation) relations in eastern North America. Bull. Seismol. Soc. Am. 93 (3), 1012–1033.
Chiou, B.J., Youngs, R.R., 2008. An NGA model for the average horizontal component of peak ground motion and response spectra. Earthq. Spectra 24 (1), 173–215.
Coleman, R.G., 1993. Geological Evolution of the Red Sea.Oxford Monographs on Geology and Geophysics. Oxford University Press, New York, p. 186.
Deif, A., Al-Shijbi, Y., El-Hussain, I., Ezzelarab, M., Mohamed, A.M., 2017. Compiling an earthquake catalogue for the Arabian Plate, Western Asia. J. Asian Earth Sci. 147, 345–357.
El-Hussain, I., Deif, A., Al-Jabri, K., Toksoz, N., El-Hady, S., Al-Hashmi, S., Al-Toubi, K., Al-Shijbi, Y., Al-Saifi, M., Kuleli, S., 2012. Probabilistic seismic hazard maps for the sultanate of Oman. Nat. Hazards 64, 173–210.
Gitis, V.G., Derendyaev, A.B., 2019. Machine learning methods for seismic hazards forecast. Geosciences 9 (7), 308.
Grünthal, G., Leydecker, F., 1993. Seismic hazard in Germany. In: InThe Practice of Earthquake Hazard Assessment. pp. 121–128. (International Association of Seismology and Physics of the Earth's Interior and European Seismological Commission).
Icold, 1989. Selecting seismic parameters for large dams. Int. Comm. Large Dams. Bull. 72, 73.
Jena, R., Shanableh, A., Al-Ruzouq, R., Pradhan, B., Gibril, M.B.A., Khalil, M.A., Ghorbanzadeh, O., Ganapathy, G.P., Ghamisi, P., 2023. Explainable artificial intelligence (XAI) model for earthquake spatial probability assessment in Arabian peninsula. Rem. Sens. 15 (9), 2248.
Jena, R., Pradhan, B., Alamri, A.M., 2020a. Susceptibility to seismic amplification and earthquake probability estimation using recurrent neural network (RNN) Model in Odisha, India. Appl. Sci. 10 (15), 5355.
Jena, R., Pradhan, B., Beydoun, G., Alamri, A.M., Sofyan, H., 2020b. Earthquake hazard and risk assessment using machine learning approaches at Palu, Indonesia. Sci. Total Environ. 749, 141582.
Johnson, P.R., 1998. Tectonic Map of Saudi Arabia and Adjacent Areas. Deputy Ministry for Mineral Resources. USGS TR-98-3, Saudi Arabia.
Ke, G., Meng, Q., Finley, T., Wang, T., Chen, W., Ma, W., Ye, Q., Liu, T.Y., 2017. Lightgbm: a highly efficient gradient boosting decision tree. Adv. Neural Inf. Process. Syst. 30.
Khan, M.M., Kalyan Kumar, G., 2018. Statistical completeness analysis of seismic data. J. Geol. Soc. India 91, 749–753.
Khan, Z., El-Emam, M., Irfan, M., Abdalla, J., 2013. Probabilistic seismic hazard analysis and spectral accelerations for United Arab Emirates. Nat. Hazards 67, 569–589.
Lenhardt, W.A., 1995,. Regional Earthquake Hazard in Austria. In10th European Conference on E*arthquake Engineering*, Balkema, Vienna, Austria, pp. 63–68. Rotterdam.

Liu, R., Li, L., Pirasteh, S., Lai, Z., Yang, X., Shahabi, H., 2021. The performance quality of LR, SVM, and RF for earthquake-induced landslides susceptibility mapping incorporating remote sensing imagery. Arabian J. Geosci. 14, 1–15.
Macedo, L., Matos, L.M., Cortez, P., Domingues, A., Moreira, G., Pilastri, A.L., 2022,. A machine learning approach for spare parts lifetime estimation. InICAART 3, 765–772.
Malkawi, A.I.H., Barakat, S., Shanableh, A., Al Bdour, W., Omar, M., Altoubat, S., 2007. Seismic hazard assessment and mitigation of earthquake risk in United Arab Emirates. In: Of Science and Technology, Aman, Jordan and the Deanship of Research and Higher Studies. University of Sharjah, UAE, Sharjah, UAE. *Published jointly by Jordan University*.
Oliveira, C.S., Campos-Costa, A., Sousa, M.L., 2000. Definition of Seismic Action in the Context of EC-8: Topics for Discussion. In*Proceedings of the Twelfth World Conference on Earthquake Engineering*, Auckland.
Pascucci, V., Free, M.W., Lubkowski, Z.A., 2008,. Seismic hazard and seismic design requirements for the Arabian Peninsula region. In: InThe 14th World Conference on E*arthquake Engineering*.
Peiris, N., Free, M., Lubkowski, Z., Hussein, A.T., 2006,. Seismic Hazard and Seismic Design Requirements for the Arabian Gulf Region. InFirst European Conference on E*arthquake Engineering and Seismology*. *European Association* of Earthquake Engineering (EAEE) Geneva, Switzerland, pp. 4–6.
Pourghasemi, H.R., Gayen, A., Panahi, M., Rezaie, F., Blaschke, T., 2019. Multi-hazard probability assessment and mapping in Iran. Sci. Total Environ. 692, 556–571.
Reiter, L., 1990. Earthquake Hazard Analysis. Columbia University Press, New York, p. 254.
Ribeiro, M.T., Singh, S., Guestrin, C., 2016. Model-agnostic Interpretability of Machine Learning. *arXiv preprint arXiv:1606.05386*.
Schäfer, A.M., Wenzel, F., 2019. Global megathrust earthquake hazard—maximum magnitude assessment using multi-variate machine learning. Front. Earth Sci. 136.
Schenk, V., Schenková, Z., Kottnauer, P., Guterch, B., Labák, P., 2000. Earthquake Hazard for the Czech Republic, Poland and Slovakia—Contribution to the ILC/IASPEI Global Seismic Hazard Assessment program.*Natural Hazards: State-Of-The-Art at the End of the Second Millennium*. pp. 331–345.
Shama, A.A., 2011. Site specific probabilistic seismic hazard analysis at Dubai Creek on the west coast of UAE. Earthq. Eng. Eng. Vib. 10 (1), 143.
Sigbjornsson, R., Elnashai, A.S., 2006. Hazard assessment of Dubai, United Arab Emirates, for close and distant earthquakes. J. Earthq. Eng. 10 (5), 749–773.
Silva-Lopez, R., Baker, J.W., Poulos, A., 2022. Deep learning–based retrofitting and seismic risk assessment of road networks. J. Comput. Civ. Eng. 36 (2), 04021038.
Stoyanov, T., 1993. Seismic hazard in Bulgaria. In: McGuire, R.K. (Ed.), The Practice of Earthquake Hazard Assessment, *International Association of Seismology and Physics of the Earth's Interior and European Seismological Commission*. p. 284.
Sulstarova, E., Koçiaj, S., Aliaj, S.H., 1980. Seismic Regionalization of the PSR of Albania.the Academy of Sciences of the People's Socialist Republic of Albania. Seismological Centre, Tirana, p. 680.
Sun, X., Liu, M., Sima, Z., 2020. A novel cryptocurrency price trend forecasting model based on LightGBM. Finance Res. Lett. 32, 101084.
Wang, Z., 2008,. Understanding seismic hazard and risk: a gap between engineers and seismologists. In: InThe 14th World Conference on E*arthquake Engineering*.
Xu, S., Niu, R., 2018. Displacement prediction of Baijiabao landslide based on empirical mode decomposition and long short-term memory neural network in Three Gorges area, China. Comput. Geosci. 111, 87–96.
Youngs, R.R., Chiou, S.J., Silva, W.J., Humphrey, J.R., 1997. Strong ground motion attenuation relationships for subduction zone earthquakes. Seismol Res. Lett. 68 (1), 58–73.
Zhao, J.X., Zhang, J., Asano, A., Ohno, Y., Oouchi, T., Takahashi, T., Ogawa, H., Irikura, K., Thio, H.K., Somerville, P.G., Fukushima, Y., 2006. Attenuation relations of strong ground motion in Japan using site classification based on predominant period. Bull. Seismol. Soc. Am. 96 (3), 898–913.